Doctoral Dissertation (Censored)

博士論文（要約）

Atomically Precise Gold Clusters Stabilized by Polyvinylpyrrolidone: Synthesis, Structural Analysis, and Catalysis

(ポリビニルピロリドン保護金クラスターの
原子精度合成、構造解析及び触媒作用)

A Dissertation Submitted for the Degree of Doctor of Philosophy

December 2021

令和 3 年 12 月博士（理学）申請

Department of Chemistry, Graduate School of Science,

The University of Tokyo

東京大学大学院理学系研究科化学専攻

Shingo Hasegawa

長谷川　慎吾

Abstract

Metal clusters smaller than a critical dimension of ~2 nm are known to exhibit unique chemical properties which cannot be predicted from those of bulk and nanoparticles of corresponding metal. To take full advantage of the size-specific chemical properties, it is essential to control the cluster size with atomic precision. Atomically precise synthesis of Au clusters has been achieved by using protecting ligands such as phosphines, *N*-heterocyclic carbenes, halides, thiolates, and alkynyls. However, these ligand-protected Au clusters are in general catalytically inactive due to the full coverage of the cluster surface. Stabilization by polymers is suitable for the catalytic applications of metal clusters, since the surface of clusters is inevitably exposed owing to the bulkiness of polymers. It has been demonstrated that Au clusters stabilized by polyvinylpyrrolidone (Au:PVP) show size-specific and high catalytic activities for oxidation reactions. The major challenges for the polymer-stabilized Au clusters are the atomically precise size control and structural determination, because the post-synthetic isolation methods and single crystal X-ray diffractometry (SCXRD) are not applicable due to the weak Au–polymer interactions and polydisperse structure of polymer layers. In my doctoral study, I achieved the kinetically controlled synthesis of new magic clusters of Au_{24}, $Au_{23}Pd_1$, and Au_{38} stabilized by PVP, as demonstrated by matrix-assisted laser desorption/ionization (MALDI) mass spectrometry. I investigated the structures of clusters by aberration-corrected transmission electron microscopy (ACTEM), X-ray absorption spectroscopy (XAS), and density functional theory (DFT) calculations. Based

on the kinetic studies of aerobic oxidation of alcohols catalyzed by Au_{24}, $Au_{23}Pd_1$, and Au_{38}, the effects of single Pd atom doping and size increase on the oxidation catalysis were discussed.

In Chapter 1, I described the general introduction of the metal clusters and catalytic applications of polymer-stabilized metal clusters. Previous works on the catalysis of polymer-stabilized metal clusters were explained with the focus on the correlation between structural parameters and catalytic performances.

In Chapter 2, I achieved the atomically precise synthesis of Au_{24}:PVP by microfluidic mixing and a large amount of PVP. According to ACTEM and theoretical calculations, the atomic structure of Au_{24}:PVP was polydisperse and fluxional. Au_{24}:PVP catalyzed the aerobic oxidation of benzyl alcohol with an apparent activation energy of 56 ± 3 kJ mol^{-1}. Kinetic isotope effect (KIE) for the α-hydrogen of benzyl alcohol and substituent effects on reaction rate constants indicated that the rate-determining step of the alcohol oxidation was the hydride elimination from the α-carbon of alcohol by Au_{24}:PVP.

In Chapter 3, I conducted the single Pd atom doping into Au_{24}:PVP by co-reduction method to obtain $Au_{23}Pd_1$:PVP. XAS, infrared spectroscopy, and DFT calculations revealed that the Pd atom was exposed on the surface of $Au_{23}Pd_1$ core. The single Pd atom doping significantly reduced the apparent activation energy for the benzyl alcohol oxidation from 56 ± 3 kJ mol^{-1} to 45 ± 2 kJ mol^{-1}. On the other hand, the observed KIE value suggested that the hydride elimination is also rate-determining for the alcohol

oxidation catalyzed by $Au_{23}Pd_1$:PVP. I proposed that the exposed Pd dopant enhances the oxidation catalysis by acting as an active site for the hydride elimination.

In Chapter 4, I successfully synthesized Au_{38}:PVP by the size conversion of the mixture of Au_{34} and Au_{43} clusters stabilized by PVP. I revealed the polydisperse and dynamic nature of the atomic structure of Au_{38}:PVP by ACTEM and theoretical calculations. Au_{38}:PVP showed the significantly higher catalytic activity than that of Au_{24}:PVP for the benzyl alcohol oxidation, whereas the KIE suggested that the rate-determining step for Au_{38}:PVP is hydride elimination. The increased affinity of Au_{38} toward a hydride might contribute to the higher catalytic activity, as suggested by DFT calculations.

In Chapter 5, I summarized the thesis and described the possible future prospects for the polymer-stabilized metal clusters.

Contents

Chapter 1.

General Introduction

1.1 Metal Nanoparticles and Clusters

Metal nanoparticles (NPs) have been used as heterogeneous and homogeneous catalysts.[1–8] An advantage of the use of metal NPs is the high proportion of surface metal atoms that can directly take part in the catalytic reactions. The catalytic activity and selectivity of metal NPs can be designed based on the chemical properties of model surfaces and interfaces, because the catalytic performances originate from reactivities of metal nanoparticles' surface and interface with support.

In contrast to the metal NPs whose catalysis is scalable with respect to the particle diameters, metal clusters smaller than a critical dimension of ~2 nm show novel chemical properties which cannot be predicted from those of bulk and NPs.[9–12] The emergence of unique catalytic properties of metal clusters is derived from the unique atomic packing and discrete electronic structures (**Figure 1.1**).

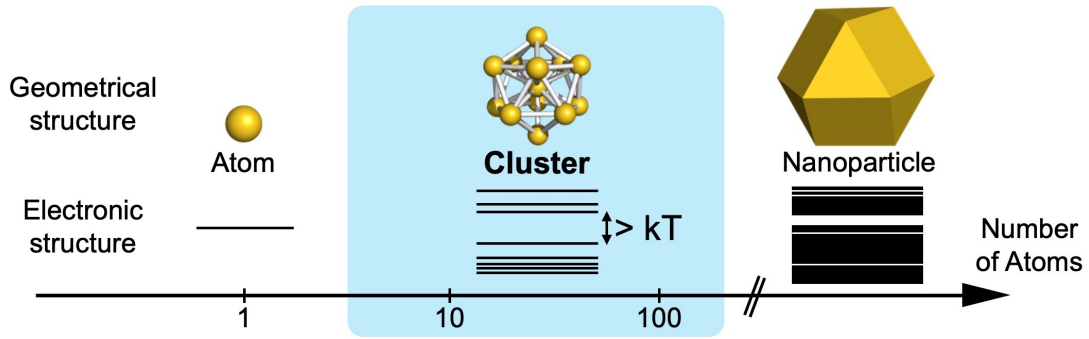

Figure 1.1. Unique atomic packing and discrete electronic structure of metal clusters.

Gas-phase studies have revealed the fundamental properties of isolated metal clusters;[13] stability,[14,15] structure,[16–22] ionization potential (IP),[23] electron affinity (EA),[24] and reactivity with small molecules.[25–27] The size-dependent behavior of the stability, IP, and EA of alkali and coinage metal clusters has been successfully explained by the jellium model qualitatively. In the model, ionic cores (nuclei and inner shell electrons) are replaced by a uniform positive charge density and valence electrons (e.g. 6s electrons for

Au) are delocalized over the corresponding potential. This theoretical treatment results in the formation of electronic shell structure accommodating the valence electrons, although details depend on the shape of an applied model potential. For instance, Woods-Saxon potential, a representative spherical jellium potential, forms the electronic shells such as 1S, 1P, 1D, 2S, 1F, 2P, and 1G in the order of energy. These shells are closed when the number of valence electrons is 2, 8, 18, 20, 34, 40, and 58, respectively. Magic numbers observed in the mass spectra of Au cluster cations and anions agreed well with the theoretical prediction.[14,15]

The geometrical structures of isolated Au clusters have been studied by ion mobility mass spectrometry (IMMS),[16,17] photoelectron spectroscopy (PES),[18–20] infrared multiphoton dissociation (IRMPD),[21] and trapped ion electron diffraction (TIED)[22] with the help of density functional theory (DFT) calculations. It is known that the unique structures of Au clusters (**Figure 1.2**) are strongly associated with the relativistic effect.[28,29] The relativistic effect contracts and stabilizes s-orbitals, which in turn destabilizes d-orbitals by the shielding of nuclear charge. The reduced energy difference

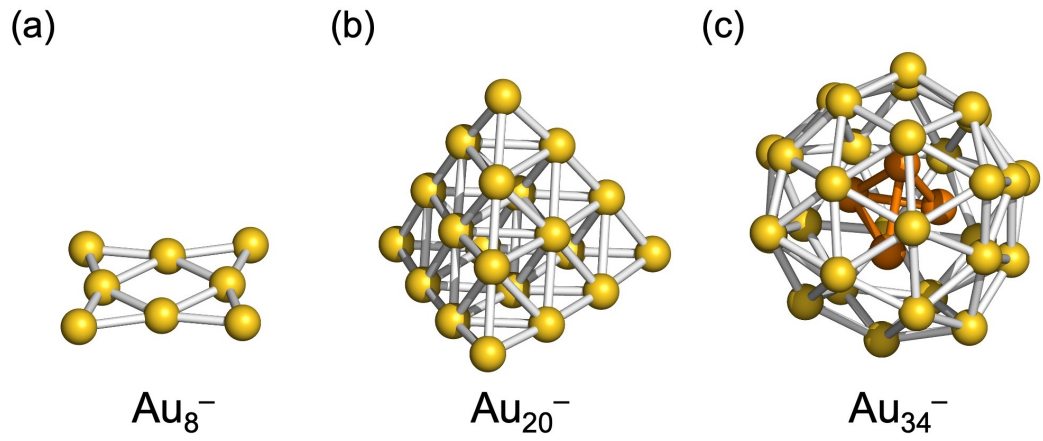

Figure 1.2. Geometrical structures of negatively charged magic number Au clusters, (a) Au_8^-, (b) Au_{20}^-, and (c) Au_{34}^-, proposed by gas-phase studies.[17,18,22] Four inner Au atoms of Au_{34}^- are colored by orange.

between 5d and 6s electrons of Au induces the s-d hybridization. Planar structures of small Au clusters (Au_n, $n < 13$) and disordered structures of medium-sized Au clusters (Au_m, $m < 64$) are ascribed to the directionality of bonding caused by the s-d hybridization.[19,30]

1.2. Catalysis of Polymer-Stabilized Metal Clusters

For the catalytic applications of metal clusters, it is necessary to prevent the aggregation of clusters while exposing the surface metal atoms as active sites for catalysis. There are three methods for the stabilization of metal clusters; protection by ligands,[10] immobilization on solid supports,[31,32] and stabilization by polymers.[33] There are both benefits and drawbacks for each method.

Ligand protection enables the atomically precise control of the sizes and compositions of metal clusters and structural determination by single crystal X-ray diffractometry (SCXRD).[34,35] However, ligand-protected metal clusters are in general catalytically inactive due to the full coverage of the surface of metal core.

Immobilization on solid supports is a suitable method for the practical catalytic applications of metal clusters, since the use of solid supports improves the robustness of clusters and the ease of the recovery of catalysts. Although the atomically precise synthesis of supported metal clusters is possible by the calcination of ligand protected metal clusters immobilized on a support under the carefully optimized conditions,[9,31,36] geometrical structures of resultant clusters and interfacial structures between supports and them are not uniform due to the heterogeneity of the surface structures of supports.

Stabilization by polymers through non-covalent interactions is an ideal approach to study the intrinsic catalysis of metal clusters.[33] Polymers prevent the aggregation of the

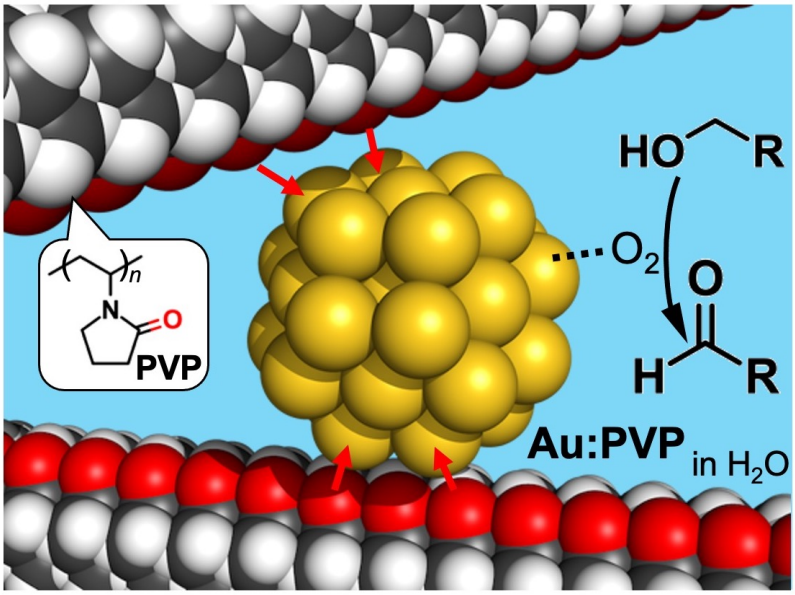

Figure 1.3. Schematic image of the coordination of polymers to a metal cluster. An Au cluster stabilized by polyvinylpyrrolidone (Au:PVP) is depicted as a representative cluster. There is exposed metal surface for a catalytic reaction.

metal clusters by multiple coordination and steric hinderance between polymer chains.[1] The bulkiness of the polymers disables the full coverage and creates the exposed sites on the cluster surface that can work as active sites for catalytic reactions (**Figure 1.3**), although the surface structures of polymer-stabilized metal clusters have not been unambiguously determined by SCXRD. According to the previous studies,[37–41] the catalytic performances of the polymer-stabilized metal clusters are regulated by the structural parameters such as size, element, interfacial structure, composition, and mixing mode (**Figure 1.4**).

1.2.1. Size Effect of Au Clusters

The high catalytic potential of Au NPs for oxidation reactions was demonstrated by the pioneering works by Haruta; Au NPs supported on metal oxides such as TiO_2 were found to be highly active for the aerobic oxidation of carbon monoxide even at the

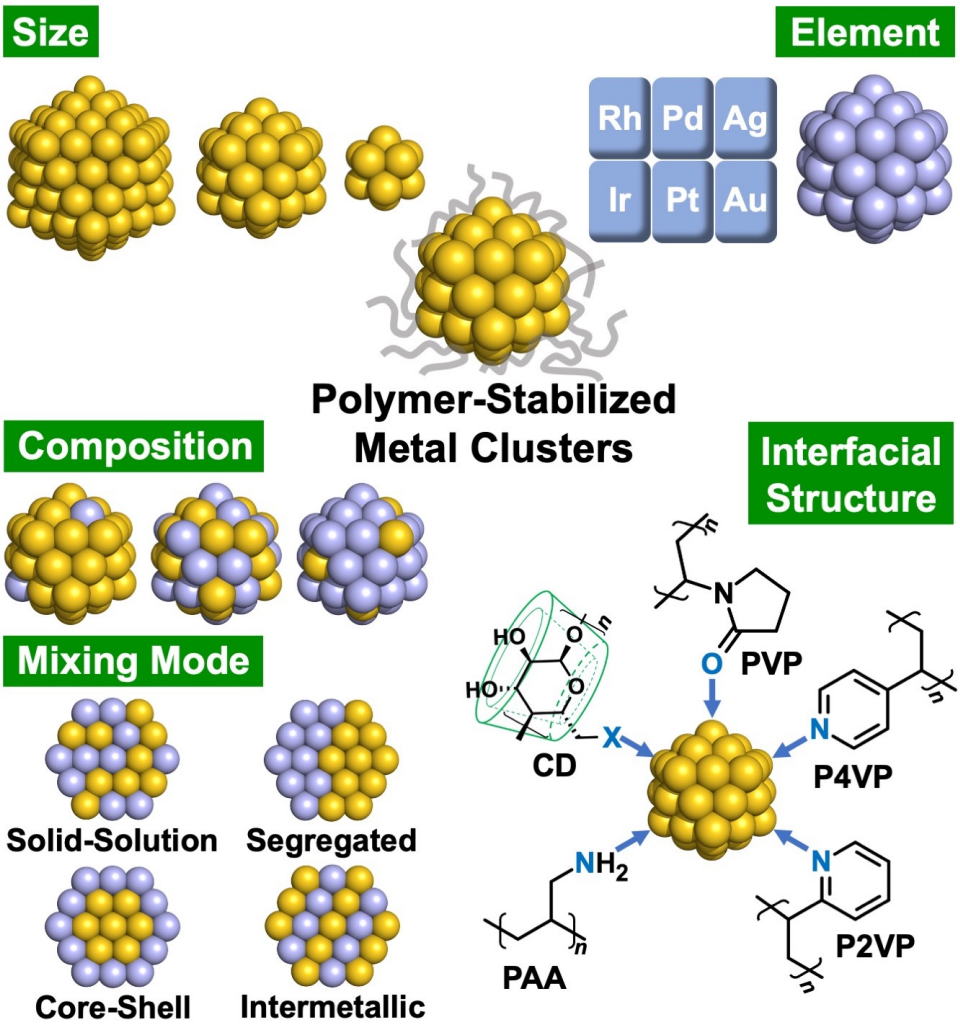

Figure 1.4. Structural parameters of polymer-stabilized metal clusters correlating with the catalysis. Abbreviations of stabilizers; polyvinylpyrrolidone (PVP), poly(4-vinylpyridine) (P4VP), poly(2-vinylpyridine) (P2VP), polyallylamine (PAA), cyclodextrin derivatives (X-(α, β, or γ)-CD) with X = OH, SH, or NH_2 (n = 6, 7, and 8 for α, β, and γ). Adapted with permission from ref. 33. Copyright 2021 The Chemical Society of Japan.

temperature of –70 °C.[42,43] As revealed by the extensive studies over decades, the active site of the supported Au catalysts is the interface between the Au particles and metal oxide supports.[44,45] Molecular oxygen is adsorbed and activated at the periphery region and reacts with carbon monoxide delivered from support and Au nanoparticles. In this

mechanism, the essential roles of Au nanoparticles are to activate the adsorbed O_2 with support and to deliver CO from the gas phase to the active sites. Therefore, it seemed that the catalytic activity of Au NPs was scalable with respect to the length of perimeter.

In 2005, it was reported that Au clusters stabilized by polyvinylpyrrolidone with average molecular weight of 40 kDa (~360 monomer units), Au:PVP, dispersed in water showed size-specific catalysis for the aerobic oxidation of *p*-hydroxybenzyl alcohol (**Scheme 1.1**);[46] the catalytic activity of Au:PVP with diameter of 1.3 nm was much higher than that of larger (9.5 nm) Au NPs stabilized by PVP. The small clusters were prepared by the rapid reduction of $HAuCl_4$ by $NaBH_4$ in the presence of 100 equivalence of PVP, whereas the large NPs were obtained by using milder reducing agent, Na_2SO_3. The catalytic reaction required the base such as K_2CO_3 and selectively produced *p*-hydroxybenzaldehyde (**2a**). On the other hand, the main products of the oxidation of other primary alcohols catalyzed by Au:PVP were carboxylic acids.[47] Moreover, Au:PVP showed higher activity than those of Pd:PVP with comparable diameters of 1.5 nm and 2.2 nm.

In the following report, the size effect on the oxidation catalysis of Au:PVP was further studied by employing the seed-growth method to finely control the size of clusters.[48] Au:PVP with homogeneous size distributions and different average diameters were prepared by reducing $AuCl_4^-$ by Na_2SO_3 in the presence of seed Au:PVP (1.3 ± 0.3 nm). Surprisingly, the reaction rate constants of the aerobic oxidation of **1a** catalyzed by Au:PVP normalized by surface area dramatically increased with the decrease of particle diameters in the small size region (**Figure 1.5**), suggesting the presence of threshold diameter of ~3 nm for the emergence of high catalytic activity. It was thought that the non-scalable behavior of the catalytic activity was associated with the discrete electronic

Scheme 1.1. Aerobic oxidation of *p*-hydroxybenzyl alcohol (**1a**) catalyzed by Au:PVP and Pd:PVP

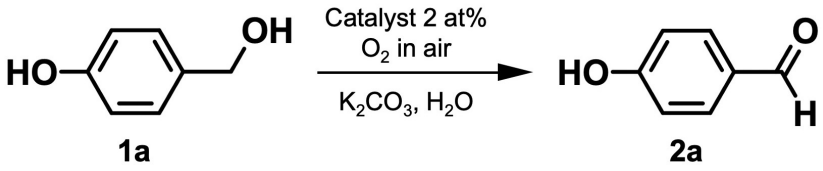

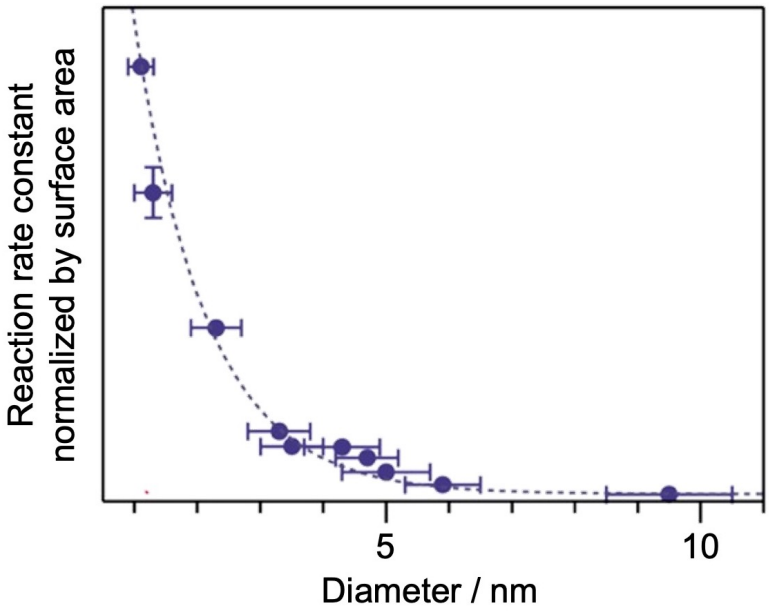

Figure 1.5. Size specific catalytic activities of Au:PVP for aerobic oxidation of **1a**. Adapted with permission from ref. 49. Copyright 2009 American Chemical Society.

structures.

The size specific aerobic oxidation catalysis of Au:PVP was attributed to the negative charge on Au cluster core provided by PVP, based on the spectroscopic observations and the high reactivity of small naked Au cluster anions, Au_n^-, toward oxygen molecules revealed by gas phase studies.[25,49] X-ray photoelectron spectroscopy (XPS), Fourier-transform infrared (FT-IR) spectroscopy of adsorbed carbon monoxide, and Au L_3-edge X-ray absorption near edge structure (XANES) of Au:PVP indicated the correlation between negative charge density on Au clusters and catalytic activity for alcohol oxidation. The reactivities of Au_n^- to molecular oxygen were highly size dependent and

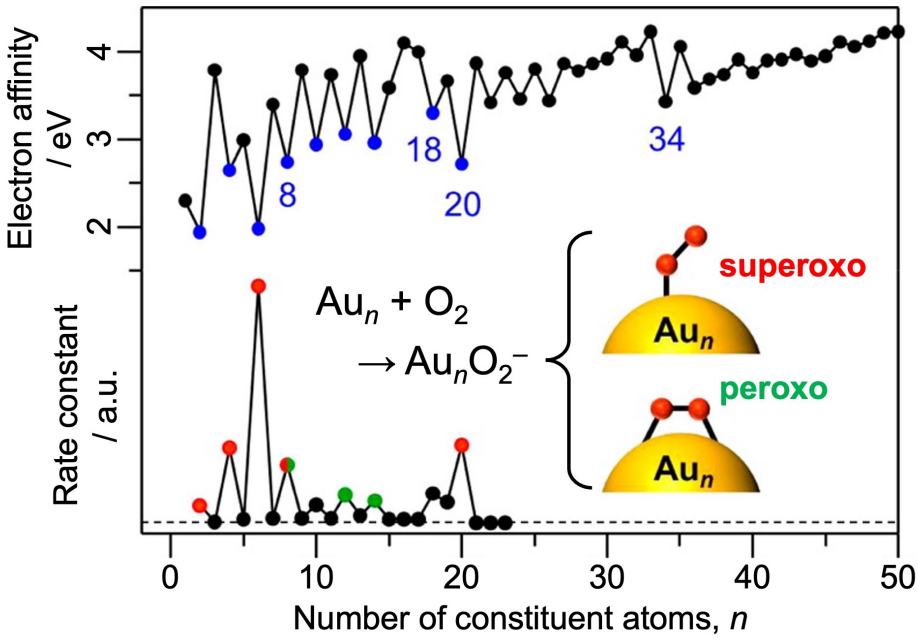

Figure 1.6. Correlation between the electron affinity of Au_n and reactivity of Au_n^- toward an O_2 molecule. Adapted with permission from ref. 9. Copyright 2013 American Chemical Society.

strongly correlated with the electron affinity of neutral forms (**Figure 1.6**).[24,25] Even numbered Au_n^-, except for n = 16, showed much larger reaction rates for the formation of adducts, $Au_nO_2^-$, than those of odd numbered anionic, neutral, or cationic clusters. Since the binding energy of the singly occupied molecular orbital (SOMO) of reactive Au_n^- was low, it seemed that the adsorbed O_2 was activated by electron transfer from the SOMO of Au_n^- to lowest unoccupied molecular orbital (LUMO) of O_2.[50] Furthermore, photoelectron spectroscopic study of $Au_nO_2^-$ reported by Pal *et al*. revealed the adsorption modes of O_2; for n = 2, 4, 6, 8, and 20 (red points in **Figure 1.6**), O_2 was activated to form superoxo-like species, whereas peroxo-like species were generated for n = 8, 12, and 14 (green points in **Figure 1.6**).[26] Based on these similarities between observations in liquid and gas phase, the reaction mechanism of alcohol oxidation catalyzed by Au:PVP was proposed; the superoxo-like species on Au:PVP formed by the reductive activation of

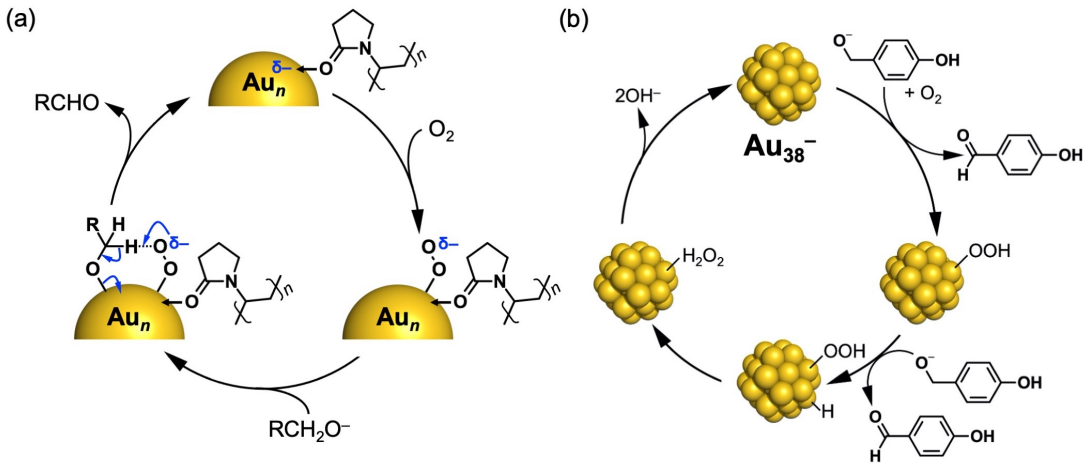

Figure 1.7. (a) Proposed reaction mechanism of aerobic alcohol oxidation catalyzed by Au:PVP.[49,51] (b) Most plausible catalytic cycle of aerobic oxidation of *p*-hydroxybenzyl alcohol catalyzed by model Au_{38}^- cluster simulated by DFT calculations.[52]

adsorbed O_2 abstracts an α-hydrogen from a co-adsorbed alkoxide (**Figure 1.7a**). It was revealed by theoretical studies that the side chain of PVP coordinated to Au clusters by carbonyl oxygen and donated electronic charge, supporting the proposed reaction mechanism.[51] Furthermore, Okumura has recently reported the detailed theoretical study on the reaction mechanism of the aerobic oxidation of **1a** catalyzed by model Au_{38}^- cluster.[52] The most energetically plausible catalytic cycle is illustrated in **Figure 1.7b**. In the cycle, the first oxidation of **1a** proceeded by the hydrogen abstraction by an adsorbed oxygen molecule, which agreed with the mechanism proposed for Au:PVP (**Figure 1.7a**). On the other hand, the second alcohol molecule was not oxidized through the hydrogen abstraction by OOH intermediate but through the hydride elimination by the cluster surface. After the oxidation of two alcohol molecules, the model cluster catalyst was recovered by the decomposition of adsorbed hydrogen peroxide.

1.2.2. Effect of Cluster Composition

1.2.2.1. Synthesis of Bimetallic Clusters

Bimetallic clusters have been prepared by various synthetic methods such as co-reduction method, seed-growth method, galvanic replacement, and controlled coalescence.[53–60] In general, the co-reduction method is suitable for the synthesis of solid solution alloy clusters, whereas the other methods tend to produce core-shell or segregated phase structures.

As demonstrated by Kitagawa and co-workers, the stability of phase structures significantly changes with the size of particles.[61] They have successfully prepared the solid solution alloy NPs composed of metal elements that are immiscible in the bulk state. For example, the synthesis of Pd-Ru solid solution alloy NPs stabilized by PVP was achieved by the polyol reduction of K_2PdCl_4 and $RuCl_3$ using triethylene glycol, although the bulk Pd and Ru are immiscible throughout the whole composition range at any temperatures up to the melting point of Pd.[37] Thus, the mixing behavior on the nanoscale does not always obey the phase diagram of corresponding bulk system probably due to the surface energy.

Toshima proposed the sacrificial hydrogen reduction method, which can be viewed as a type of seed-growth method, for the synthesis of Pd-Pt core-shell clusters stabilized by PVP.[53] In the report, K_2PtCl_4 was reduced by surface hydrogen atoms on Pd:PVP generated by the dissociative adsorption of molecular hydrogen. Owing to the much higher reducing ability of the surface hydrogen atoms than those of dissolved hydrogen molecules, Pt atoms were successfully deposited on the surface of Pd clusters and Pd-Pt core-shell clusters were obtained in controllable manner.

Galvanic reaction was used by Toshima and co-workers to introduce Au atoms to the

corner sites of Pd:PVP, as illustrated in **Figure 1.8a**.[54] Based on the relative stability of corner, edge, and facet atoms, it was expected that the galvanic replacement on the surface of Pd:PVP first occurred from the corner Pd atoms. Formation of the crown jewel (CJ) structure was concluded from the observation of AuPd:PVP by High-angle annular dark-field scanning transmission electron microscopy (HAADF-STEM).

Sakurai reported the size-control of Au-Pd clusters and NPs by the time-controlled aggregation method (**Figure 1.8b**).[60] In contrast to the case of monometallic clusters,[48] it is difficult to apply seed-growth method to control the size of bimetallic clusters while keeping the composition. The proposed method was composed of two steps; (1) the formation of homogeneous and small seed Au-Pd clusters by the co-reduction of precursor metal complexes ($HAuCl_4$ and H_2PdCl_4) and (2) coalescence of the seed

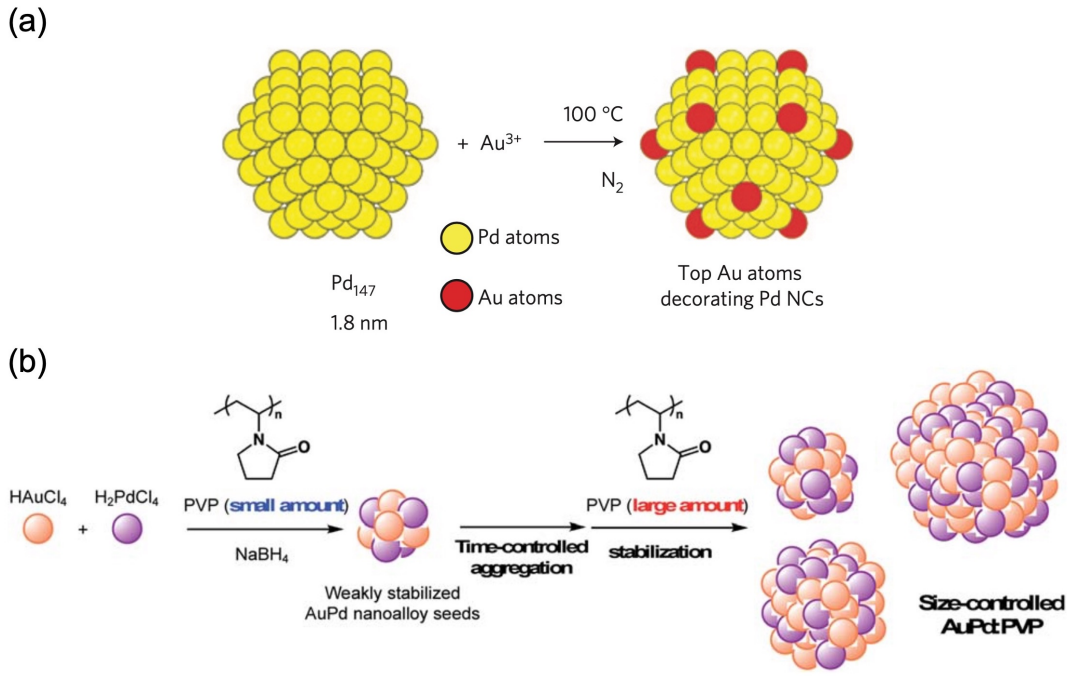

Figure 1.8. (a) Preparation of Au-Pd CJ clusters stabilized by PVP by galvanic replacement of Pd by Au. (b) Synthesis of Au-Pd solid solution clusters stabilized by PVP with different particle sizes by controlled coalescence. (a) Adapted with permission from ref. 54. Copyright 2012 Macmillan Publishers Limited. (b) Adapted with permission from ref. 60. Copyright 2021 Royal Society of Chemistry.

clusters with different times quenched by additional PVP. On the other hand, the formation of bimetallic (Au-Ag, Ag-Rh, Ag-Pd, and Ag-Pt) clusters and NPs by physical mixing of monometallic particles was reported by Toshima.[55,58] The physical mixing between large Ag:PVP (10 nm) and small (2.0–3.5 nm) M:PVP (M = Rh, Pd, and Pt) produced Ag-M core-shell NPs. Based on the results of kinetic measurements, it was proposed that the inter-particle reaction is initiated by electron transfer from Ag:PVP to M:PVP.

1.2.2.2. Catalysis of Bimetallic Clusters

It has been demonstrated that the introduction of heterometal element is a promising approach to improve the catalytic performances of metal clusters.[62–70] The catalysis of Au-based alloy clusters stabilized by PVP has been extensively studied. In the report by Chaki *et al*., Ag-doped Au:PVP were synthesized by the co-reduction of $HAuCl_4$ and $AgNO_3$ at Ag doping amount of 5–30 at%.[62] The reaction rate constant of the aerobic oxidation of **1a** (**Scheme 1.1**) normalized by the surface area was enhanced by the Ag doping and maximized by 10 at% doping. The higher catalytic activity of AuAg:PVP was attributed to the enhanced negative charge density on Au atoms resulted from the intra-cluster charge transfer between Au and Ag atoms. This conclusion was consistent with the proposed reaction mechanism (**Figure 1.7a**) in which electron-rich Au atoms act as active centers for the catalytic oxidation.[49] However, the impact of particle size on the catalytic activity could not be excluded; the estimated average diameters of AuAg:PVP increased from 1.3 to 2.2 nm with the increase of Ag content from 0 to 30 at%.

It was demonstrated by Nakajima that the Au-Pd alloy clusters stabilized by PVP could be synthesized within the whole composition range while retaining the cluster size

Scheme 1.2. (a) Aerobic oxidation of benzyl alcohol (**1b**) catalyzed by AuPd:PVP. (b) Aerobic oxidation of glucose (**1c**) catalyzed by CJ-structured AuPd:PVP. (c) Ullmann coupling reaction of 4-chlorotoluene (**1d**) catalyzed by AuPd:PVP.

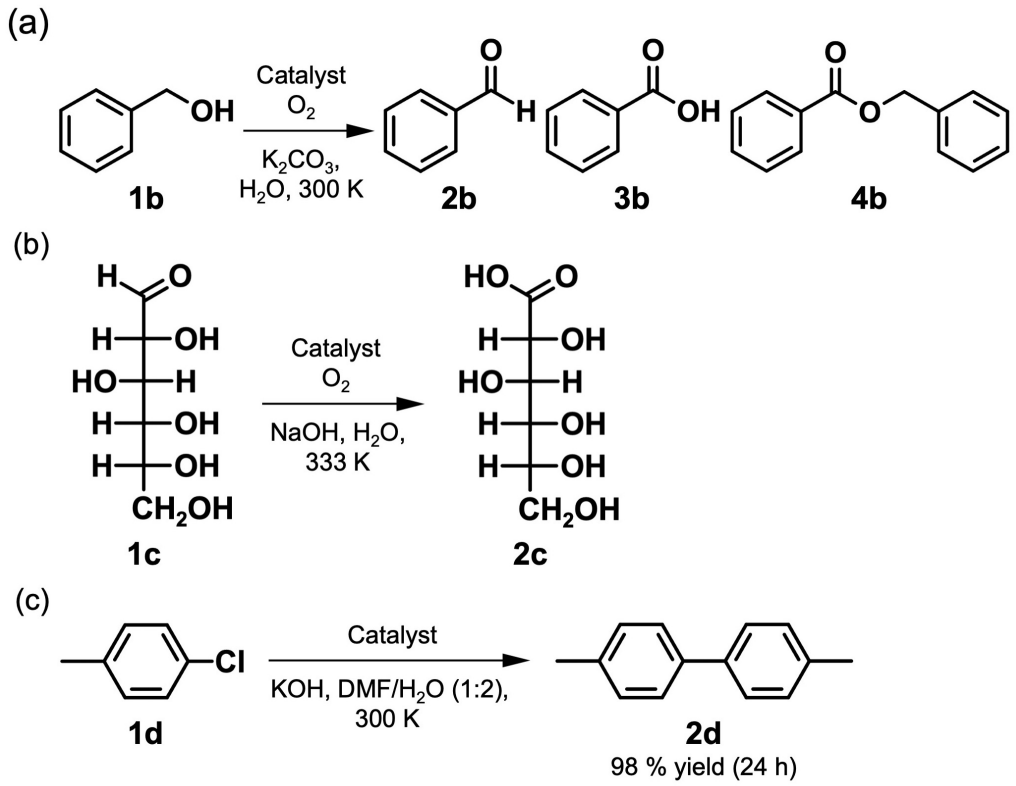

using a microfluidic mixier.[65] AuPd:PVP were synthesized by microfluidic mixing of an aqueous solution of $HAuCl_4$, H_2PdCl_4, and PVP with that of $NaBH_4$ and PVP. Thus synthesized bimetallic clusters showed solid solution structures and homogeneous size distributions with mean diameter of 1.0–1.7 nm. The catalytic activity of AuPd:PVP dispersed in water for the aerobic oxidation of benzyl alcohol (**Scheme 1.2a**) was higher than those of Au:PVP and Pd:PVP, which was ascribed to the electronic charge transfer from Pd atoms to neighboring Au atoms.

Toshima reported that the CJ-structured AuPd:PVP (**Figure 1.8a**) showed remarkably high turnover frequency (TOF) of 194980 $mol_{glucose}$ h^{-1} mol_{Au}^{-1} for the aerobic oxidation of glucose (**Scheme 1.2b**).[54] Under the reported reaction condition,

glucose (**1c**) was selectively converted to gluconic acid (**2c**). Based on the results of XPS and DFT calculations of model clusters, it was concluded that negatively charged Au dopants on Pd clusters were responsible for the high catalytic activity. Moreover, the catalytic activity of CJ-structured AuPd:PVP was further enhanced by the introduction of Ir to the Pd cluster core, in the following report.[56] Au atoms were introduced to the corner sites of PdIr:PVP by a similar synthetic method. TOF as high as 343190 $mol_{glucose}$ h^{-1} mol_{Au}^{-1} was achieved by the CJ-structured AuPdIr:PVP.

Sakurai demonstrated the emergence of novel catalysis by the synergistic effect between Au and Pd atoms of AuPd:PVP.[63,64,67] It was found that AuPd:PVP dispersed in DMF/H_2O (1:2) efficiently catalyzed the homocoupling reactions of various chloroarenes (Ullmann coupling reactions) under mild reaction conditions (**Scheme 1.2c**), whereas monometallic counterparts and their physical mixture showed no catalytic activity. The large kinetic isotope effect (k_H/k_D = 7.0) induced by DMF-d_7 indicated that the hydrogen transfer from DMF to AuPd:PVP was the rate-determining step. Theoretical studies of the reaction mechanism were carried out by Ehara.[63,71] DFT calculations revealed that the critical process was the oxidative addition of chloroarenes; a pure Au cluster showed too large activation energy for the oxidative addition, whereas the oxidative addition on a Pd cluster produced a too stable reaction intermediate. Only an Au-Pd cluster showed a feasible energy profile. In Ullmann coupling reactions catalyzed by AuPd:PVP, the active metal was Pd and the essential role of Au was to facilitate the migration of surface chloride and to prevent the deactivation processes such as the leaching of Pd.[67]

1.2.3. Effect of Interfacial Structure

As explained in **1.2.1**, the negative charge on Au clusters provided by PVP played a

Scheme 1.3. (a) Aerobic oxidation of 1-indanol catalyzed by Au:PVP with different chain lengths of PVP. (b) Aerobic oxidation of 1-octanol catalyzed by Au:P4VP (1.1 ± 0.2 nm), Au:P2VP (1.1 ± 0.2), and Au:PVP (1.0 ± 0.2 nm).

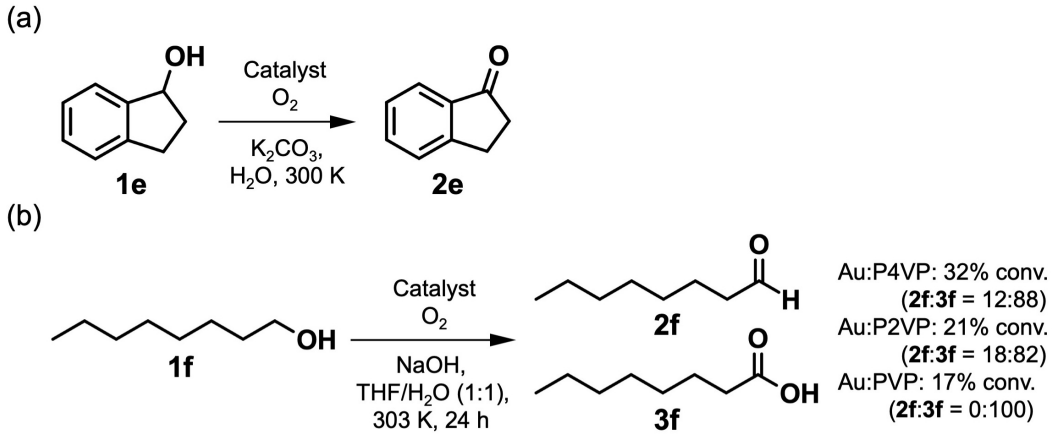

crucial role in the aerobic oxidation catalysis of Au:PVP by reductively activating the adsorbed O_2 molecules (**Figure 1.7a**).[49] Thus, the catalysis of polymer-stabilized metal clusters is affected not only by the steric hinderance of polymers but also through the modulation of electronic structure by polymers.

In a recent study reported by Sakurai, it was found that the size-dependence of catalytic activities of Au:PVP for the aerobic oxidation of 1-indanol (**Scheme 1.3a**) depended on the chain length of PVP.[72] Au:PVP were prepared by using PVP with different molecular weight; PVP K-30 (~40 kDa, ~360 monomers), PVP K-60 (~160 kDa, ~1440 monomers), and PVP K-90 (~360 kDa, ~3240 monomers). For each chain length, the core size of Au:PVP was controlled over the range between ~1 nm and ~9 nm. The highest catalytic activity was shown by Au:PVP (K-90) with the core size of ~7 nm, which was much higher than those of smaller particles. This unexpected behavior of the size dependence of catalytic activities was attributed to the high negative charge density on the surface of large NPs caused by the dense packing of polymer layers.

Poly(4-vinylpyridine) (P4VP) and Poly(2-vinylpyridine) (P2VP) illustrated in

Figure 1.4 have been recently introduced as electron-donating stabilizers for small (~1 nm) and monodisperse Au clusters.[73] For the aerobic oxidation of 1-octanol (**Scheme 1.3b**), Au:P4VP and Au:P2VP showed higher catalytic activities and smaller degrees of aggregation than those of Au:PVP, although Au:PVP was more active for the oxidation of **1b** (**Scheme 1.2a**). XPS and optical absorption spectroscopy indicated that the degree of electron donation to the Au cluster was in the order of P2VP > P4VP ~ PVP, which was supported by DFT calculations of the model system consisting of Au_{34} cluster and monomer units of the polymers. Nevertheless, the lower catalytic activity of Au:P2VP compared to that of Au:P4VP was not consistent with the trend of electron-donating ability. The discrepancy was explained by the difference of surface coverage; the closer distance between the cluster surface and the polymer chain of P2VP could induce higher surface coverage and sterically hinder the catalytic reaction. The substrate dependence of the catalytic activity was attributed to the hydrophobicity of polymers; hydrophobic P4VP and P2VP promoted the access of hydrophobic **1f** to the metal surface, whereas the accessibility of hydrophilic **1b** was higher for Au:PVP. The improved robustness of Au:P4VP and Au:P2VP revealed by TEM was ascribed to larger binding energies of pyridine units than that of the pyrrolidone unit, according to DFT calculations.

1.3. Aim and Outline

It has been demonstrated that Au:PVP show size-specific and high catalytic activity for the aerobic oxidation reactions.[9] On the other hand, gas-phase studies demonstrated the importance of atomically precise size control; the reactivity of Au cluster anions with molecular oxygen was highly dependent on the number of constituent atoms (**Figure 1.6**).[25] Therefore, it is essential to achieve the atomic precision in the synthesis of Au:PVP

to take full advantage of the size-specific catalysis of Au clusters.

Atomically precise synthesis of Au clusters has been achieved by employing protecting ligands such as phosphines, *N*-heterocyclic carbenes, halides, thiolates, and alkynyls.[35,74] The successful synthesis was enabled by the size-focusing by chemical etching and isolation techniques based on chromatography and fractional precipitation. However, these well-established size control methods cannot be applied to polymer stabilized Au clusters due to the fragile Au–polymer interactions and polydisperse conformations of the coordinating polymers. Another challenge for polymer-stabilized Au clusters is the determination of the atomic structure, since SCXRD is not applicable in contrast to ligand-protected Au clusters.

The aim of my doctoral study is to tackle the major challenges; atomically precise size control and determination of atomic structure. The approaches for the former are the kinetic control of cluster synthesis and the size evaluation by mass spectrometry. Recently, matrix-assisted laser desorption/ionization (MALDI) mass spectrometry has been introduced to ionize the metal core of polymer-stabilized metal clusters as an intact form and to determine the cluster size with atomic precision.[75] It was revealed that Au:PVP were the mixture of magic number Au clusters such as $Au_{35\pm1}$, $Au_{43\pm1}$, $Au_{58\pm1}$, and $Au_{70\pm3}$ (**Figure 1.9a**).[75,76] Furthermore, the microfluidic mixing (**Figures 1.9b** and **c**) was found to be effective for the kinetic control of the formation process of metal clusters; Au:PVP prepared by the homogeneous mixing of aqueous solutions of $HAuCl_4$ and $NaBH_4$ using a micromixer showed narrower size distribution than that of the sample obtained by conventional batch method (**Figure 1.9a**).[77] These results suggest the possibility of atomically precise synthesis of Au:PVP by further optimization of synthetic parameters such as the amount of PVP.

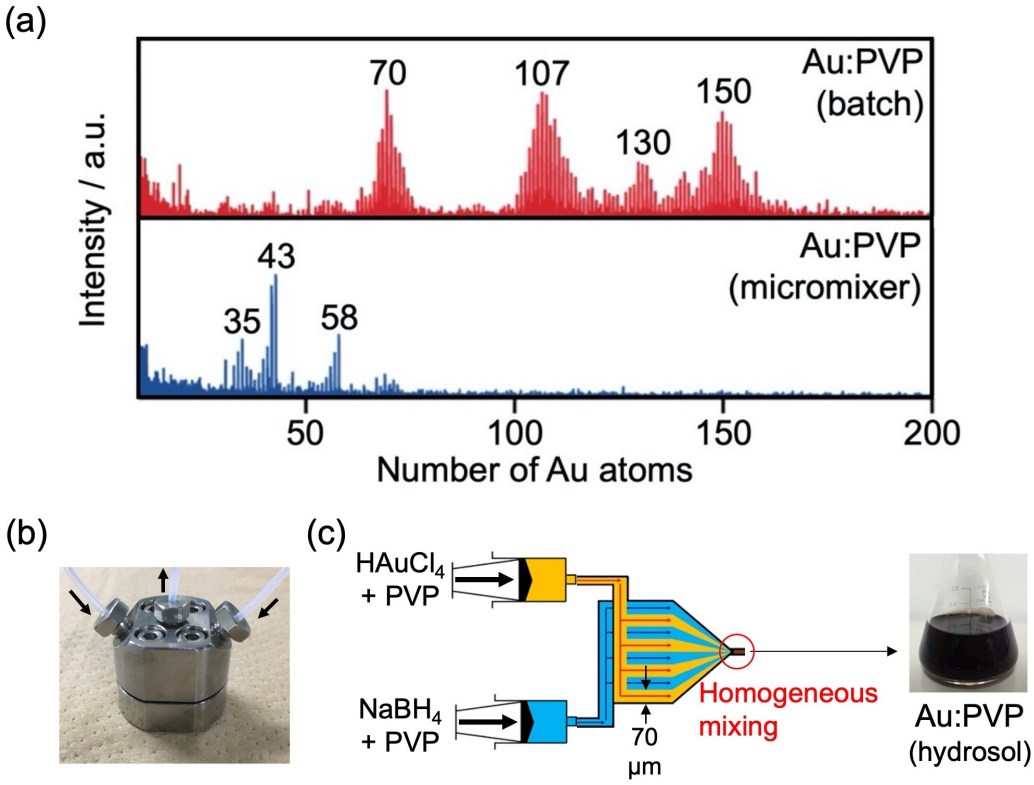

Figure 1.9. (a) MALDI mass spectra of Au:PVP prepared by conventional batch method (red) and microfluidic mixing (blue) (b) A micromixer (SIMM-V2) used for the synthesis of Au:PVP. (c) Schematic image of the microfluidic synthesis of Au:PVP. (a) Adapted with permission from ref. 75. Copyright 2009 American Chemical Society.

The issue of structural determination can be addressed by aberration-corrected transmission electron microscopy (ACTEM). Although the ACTEM images are the projection image of the object, the three-dimensional atomic structures of metal clusters can be reconstructed from the images with the help of density functional theory (DFT) calculations.[78,79] In addition to the applicability of ACTEM to samples that cannot be crystallized, another advantage is that ACTEM enables the monitoring of the dynamic behavior of the structure of individual particles with an atomic resolution. For example, ACTEM observation of supported Au NPs revealed the novel phenomena such as quasimelting,[80–82] structural isomerization,[83] and size-dependent phase transitions.[84]

In Chapter 2, I achieved the atomically precise synthesis of a novel magic number

cluster, Au_{24}:PVP, by the microfluidic mixing of reaction solutions containing a large excess of PVP. The successful synthesis was ascribed to the suppression of the growth reaction of clusters as well as the homogeneous mixing of the reaction solutions. By ACTEM video imaging of Au_{24}:PVP and TEM simulations of model Au_{24} clusters obtained by DFT calculations, I revealed that Au_{24}:PVP was the mixture of structural isomers in which all the constituent atoms were exposed on the cluster surface. Furthermore, the dynamic nature of the atomic structure of Au_{24}:PVP was demonstrated by the direct observation of structural isomerization. I found that the metal core of Au_{24}:PVP was negatively charged due to the electron transfer from PVP, according to the results of XPS and FT-IR spectroscopy of adsorbed carbon monoxide. The reaction mechanism of the aerobic oxidation of **1b** (**Scheme 1.2a**) catalyzed by Au_{24}:PVP was investigated by kinetic measurements. I concluded that the rate-determining step of the catalytic oxidation was the hydride elimination from α-carbon by Au_{24}:PVP, based on the observation of kinetic isotope effect (KIE) and substituent effects on reaction rate constants.

In Chapter 3, I demonstrated that single Pd atom could be doped into Au_{24}:PVP by the co-reduction method. $Au_{23}Pd_1$:PVP was selectively obtained by the reduction of the mixture of $HAuCl_4$ and Na_2PdCl_4 by $NaBH_4$ under the reaction condition similar to that for Au_{24}:PVP. I studied the local structure around the Pd dopant in $Au_{23}Pd_1$:PVP by Pd K-edge extended X-ray absorption fine structure (EXAFS) analysis, FT-IR spectroscopy of adsorbed carbon monoxide, and DFT calculations. Considering the coordination number of the Pd–Au bond (6.1 ± 0.7) significantly smaller than 12 and the appearance of the absorption band corresponding to the CO adsorbed on Pd, I concluded that the Pd atom was exposed on the cluster surface. The single Pd atom doping effect on the catalysis was

investigated for the oxidation of **1b**. $Au_{23}Pd_1$:PVP showed the significantly higher catalytic activity; the reaction rate constant at 303 K for $Au_{23}Pd_1$:PVP (2.3 h^{-1}) was more than 2 times higher than that for Au_{24}:PVP (0.83 h^{-1}) and the apparent activation energy was reduced by single Pd atom doping from 56 ± 3 kJ mol^{-1} to 45 ± 2 kJ mol^{-1}. On the other hand, KIE suggested that the hydride elimination from the α-carbon of benzyl alcohol is also the rate-determining step for $Au_{23}Pd_1$:PVP. Based on the structure of $Au_{23}Pd_1$:PVP where the Pd atom is exposed on the surface and high affinity of Pd toward H, it was proposed that the Pd dopant acts as a reaction site for hydride elimination with reduced activation energy.

In Chapter 4, it was found that a new magic number cluster, Au_{38}:PVP, was selectively and reproducibly obtained by the size conversion reaction of the mixture of Au_{34} and Au_{43}. I revealed the polydisperse and dynamic nature of the atomic structure of Au_{38}:PVP by ACTEM video imaging with the help of the TEM simulation of DFT-optimized model structures. DFT calculations suggested the non-crystalline geometrical structures with 0–4 inner Au atoms as stable structural isomers. The catalytic activity of Au_{38}:PVP for the oxidation of **1b** was significantly higher than that of Au_{24}:PVP. Au_{38}:PVP showed smaller apparent activation energy (48 ± 1 kJ mol^{-1}) than that of Au_{24}:PVP (56 ± 3 kJ mol^{-1}), whereas the KIE values of the clusters were comparable. This suggested that the hydride elimination is rate-determining step for both catalysts, which was supported by the result of Hammett analysis. DFT calculations revealed that Au_{38} showed larger adsorption energies to a hydride than those of Au_{24} and that the trend was more prominent for anionic clusters. I proposed that the higher capability of the Au_{38} core to accept excess negative charge is the origin of higher catalytic activity of Au_{38}:PVP for alcohol oxidation.

In Chapter 5, I summarized the achievements in Chapters 2–4 and discussed the future prospects for the polymer-stabilized metal clusters.

References

1. Toshima, N. Yonezawa, T. *New J. Chem*. **1998**, *22*, 1179.
2. Burda, C.; Chen, X.; Narayanan, R.; El-Sayed, M. A. *Chem. Rev.* **2005**, *105*, 1025.
3. Sankar, M.; Dimitratos, N.; Miedziak, P. J.; Wells, P. P.; Kiely, C. J.; Hutchings, G. J. *Chem. Soc. Rev.* **2012**, *41*, 8099.
4. Mitsudome, T.; Kaneda, K. *Green Chem.* **2013**, *15*, 2636.
5. Yasukawa, T.; Miyamura, H.; Kobayashi, S. *Chem. Soc. Rev.* **2014**, *43*, 1450.
6. Liu, L.; Corma, A. *Chem. Rev*. **2018**, *118*, 4981.
7. Ishida, T.; Murayama, T.; Taketoshi, A.; Haruta, M. *Chem. Rev.* **2020**, *120*, 464.
8. Gao, C.; Lyu, F.; Yin, Y. *Chem. Rev.* **2021**, *121*, 834.
9. Yamazoe, S.; Koyasu, K.; Tsukuda, T. *Acc. Chem. Res.* **2014**, *47*, 816.
10. Du, Y.; Sheng, H.; Astruc, D.; Zhu, M. *Chem. Rev.* **2020**, *120*, 526.
11. Kang, X.; Li, Y.; Zhu, M.; Jin, R. *Chem. Soc. Rev.* **2020**, *49*, 6443.
12. Kawawaki, T.; Negishi, Y.; Kawasaki, H. *Nanoscale Adv.* **2020**, *2*, 17.
13. de Heer, W. A. *Rev. Mod. Phys*. **1993**, *65*, 611.
14. Katakuse, I.; Ichihara, T.; Fujita, Y.; Matsuo, T.; Sakurai, T.; Matsuda, H. *Int. J. Mass Spectrom. Ion Processes* **1985**, *67*, 229.
15. Katakuse, I.; Ichihara, T.; Fujita, Y.; Matsuo, T.; Sakurai, T.; Matsuda, H. *Int. J. Mass Spectrom. Ion Processes* **1986**, *74*, 33.
16. Gilb, S.; Weis, P.; Furche, F.; Ahlrichs, R.; Kappes, M. M. *J. Chem. Phys*. **2002**, *116*, 4094.
17. Furche, F.; Ahlrichs, R.; Weis, P.; Jacob, C.; Gilb, S.; Bierweiler, T.; Kappes, M. M. *J. Chem. Phys*. **2002**, *117*, 6982.
18. Li, J.; Li, X.; Zhai, H.-J.; Wang, L. S. *Science*. **2003**, *299*, 864.
19. Huang, W.; Ji, M.; Dong, C.-D.; Gu, X.; Wang, L.-M.; Gong, X. G.; Wang, L. S. *ACS Nano* **2008**, *2*, 897.
20. Shao, N.; Huang, W.; Gao, Y.; Wang, L.-M.; Li, X.; Wang, L. S.; Zeng, X. C. *J. Am. Chem. Soc*. **2010**, *132*, 6596.
21. Gruene, P.; Rayner, D. M.; Redlich, B.; Meer, A. F. G. v. d.; Lyon, J. T.; Meijer, G.; Fielicke, A. *Science* **2008**, *321*, 674.
22. Lechtken, A.; Schooss, D.; Stairs, J. R.; Blom, M. N.; Furche, F.; Morgner, N.; Kostko, O.; Issendorff, B. v.; Kappes, M. M. *Angew. Chem., Int. Ed*. **2007**, *46*, 2944.
23. Jackschath, C.; Rabin, I.; Schulze, W. *Ber. Bunsenges. Phys. Chem.* **1992**, *96*, 1200.
24. Taylor, K. J.; Pettiette-Hall, C. L.; Cheshnovsky, O.; Smalley, R. E. *J. Chem. Phys.* **1992**, *96*, 3319.
25. Wallace, W. T.; Whetten, R. L. *J. Am. Chem. Soc.* **2002**, *124*, 7499.

26. Pal, R.; Wang, L.-M.; Pei, Y.; Wang, L. S.; Zeng, X. C. *J. Am. Chem. Soc.* **2012**, *134*, 9438.
27. Yamaguchi, M.; Miyajima, K.; Mafuné, F. *J. Phys. Chem. C* **2016**, *120*, 23069.
28. Pyykkö, P. *Chem. Rev.* **1988**, *88*, 563.
29. Pyykkö, P. *Angew. Chem., Int. Ed*. **2004**, *43*, 4412.
30. Häkkinen, H.; Moseler, M.; Landman, U. *Phys. Rev. Lett*. **2002**, *89*, 033401.
31. Yamazoe, S.; Yoskamtorn, T.; Takano, S.; Yadnum, S.; Limtrakul, J.; Tsukuda, T. *Chem*. *Rec*. **2016**, *16*, 2338.
32. Jin, R.; Li, G.; Sharma, S.; Li, Y.; Du, X. *Chem. Rev.* **2021**, *121*, 567.
33. Hasegawa, S.; Tsukuda, T. *Bull. Chem. Soc. Jpn*. **2021**, *94*, 1036.
34. Chakraborty, I.; Pradeep, T. *Chem. Rev.* **2017**, *117*, 8208.
35. Omoda, T.; Takano, S.; Tsukuda, T. *Small* **2021**, *17*, 2001439.
36. Sudheeshkumar, V.; Sulaiman, K. O.; Scott, R. W. J. *Nanoscale Adv.* **2020**, *2*, 55.
37. Kusada, K.; Kobayashi, H.; Ikeda, R.; Kubota, Y.; Takata, M.; Toh, S.; Yamamoto, T.; Matsumura, S.; Sumi, N.; Sato, K.; Nagaoka, K.; Kitagawa, H. *J. Am*. *Chem*. *Soc*. **2014**, *136*, 1864.
38. Gilroy, K. D.; Ruditskiy, A.; Peng, H.-C.; Qin, D.; Xia, Y. *Chem. Rev.* **2016**, *116*, 10414.
39. Furukawa, S.; Komatsu, T. *ACS Catal.* **2017**, *7*, 735.
40. Ma, S.; Sadakiyo, M.; Heima, M.; Luo, R.; Haasch, R. T.; Gold, J. I.; Yamauchi, M.; Kenis, P. J. A. *J. Am*. *Chem*. *Soc*. **2017**, *139*, 47.
41. Sadhukhan, T.; Junkaew, A.; Zhao, P.; Miura, H.; Shishido, T.; Ehara, M. *Organometallics* **2020**, *39*, 528.
42. Haruta, M.; Kobayashi, T.; Sano, H.; Yamada, N. *Chem. Lett*. **1987**, *16*, 405.
43. Haruta, M.; Yamada, N.; Kobayashi, T.; Iijima, S. *J. Catal.* **1989**, *115*, 301.
44. Green, I. X.; Tang, W.; Neurock, M.; Yates, J. T. *Science* **2011**, *333*, 736.
45. Fujitani, T.; Nakamura, I. *Angew. Chem., Int. Ed.* **2011**, *50*, 10144.
46. Tsunoyama, H.; Sakurai, H.; Negishi, Y.; Tsukuda, T. *J. Am*. *Chem*. *Soc*. **2005**, *127*, 9374.
47. Tsunoyama, H.; Tsukuda, T.; Sakurai, H. *Chem. Lett.* **2007**, *36*, 212.
48. Tsunoyama, H.; Sakurai, H.; Tsukuda, T. *Chem. Phys. Lett*. **2006**, *429*, 528.
49. Tsunoyama, H.; Ichikuni, N.; Sakurai, H.; Tsukuda, T. *J. Am. Chem. Soc*. **2009**, *131*, 7086.
50. Muramatsu, S.; Tsukuda, T. *Chem. Asian J.* **2019**, *14*, 3763.
51. Okumura, M.; Kitagawa, Y.; Kawakami, T.; Haruta, M. *Chem. Phys. Lett.* **2008**, *459*, 133.

52. Ato, Y.; Hayashi, A.; Koga, H.; Kawakami, T.; Yamanaka, S.; Okumura, M. *Chem. Phys. Lett.* **2019**, *724*, 115.
53. Wang, Y.; Toshima, N. *J. Phys. Chem. B* **1997**, *101*, 5301.
54. Zhang, H.; Watanabe, T.; Okumura, M.; Haruta, M.; Toshima, N. *Nat. Mater.* **2012**, *11*, 49.
55. Zhang, H.; Haba, M.; Okumura, M.; Akita, T.; Hashimoto, S.; Toshima, N. *Langmuir* **2013**, *29*, 10330.
56. Zhang, H.; Lu, L.; Kawashima, K.; Okumura, M.; Haruta, M.; Toshima, N. *Adv. Mater.* **2015**, *27*, 1383.
57. Fiévet, F.; Ammar-Merah, S.; Brayner, R.; Chau, F.; Giraud, M.; Mammeri, F.; Peron, J.; Piquemal, J.-Y.; Sicard, L.; Viau, G. *Chem. Soc. Rev.* **2018**, *47*, 5187.
58. Hirakawa, K.; Kaneko, T.; Toshima, N. *Chem. Asian J.* **2018**, *13*, 1892.
59. Matsuda, S.; Masuda, S.; Takano, S.; Ichikuni, N.; Tsukuda, T. *ACS Catal.* **2021**, *11*, 10502.
60. Uetake, Y.; Mouri, S.; Haesuwannakij, S.; Okumura, K.; Sakurai H. *Nanoscale Adv.* **2021**, *3*, 1496.
61. Kusada, K.; Kitagawa, H. *Adv. Mater.* **2016**, *28*, 1129.
62. Chaki, N. K.; Tsunoyama, H.; Negishi, Y.; Sakurai, H.; Tsukuda, T. *J. Phys. Chem. C* **2007**, *111*, 4885.
63. Dhital, R. N.; Kamonsatikul, C.; Somsook, E.; Bobuatong, K.; Ehara, M.; Karanjit, S.; Sakurai, H. *J. Am. Chem. Soc.* **2012**, *134*, 20250.
64. Dhital, R. N.; Kamonsatikul, C.; Somsook, E.; Sakurai, H. *Catal. Sci. Technol.* **2013**, *3*, 3030.
65. Hayashi, N.; Sakai, Y.; Tsunoyama, H.; Nakajima, A. *Langmuir* **2014**, *30*, 10539.
66. Sharif, M. J.; Yamazoe, S.; Tsukuda, T. *Top. Catal.* **2014**, *57*, 1049.
67. Karanjit, S.; Jinasan, A.; Somsook, E.; Dhital, R. N.; Motomiya, K.; Sato, Y.; Tohji, K.; Sakurai, H. *Chem. Commun.* **2015**, *51*, 12724.
68. Hayashi, S.; Ishida, R.; Hasegawa, S.; Yamazoe, S.; Tsukuda, T. *Top. Catal.* **2018**, *61*, 136.
69. Hasegawa, S.; Takano, S.; Yamazoe, S.; Tsukuda, T. *Chem. Commun.* **2018**, *54*, 5915.
70. Dhital, R. N.; Nomura, K.; Sato, Y.; Haesuwannakij, S.; Ehara, M.; Sakurai, H. *Bull. Chem. Soc. Jpn.* **2020**, *93*, 1180.
71. Meeprasert, J.; Namuangruk, S.; Boekfa, B.; Dhital, R. N.; Sakurai, H.; Ehara, M. *Organometallics* **2016**, *35*, 1192.
72. Haesuwannakij, S.; Kimura, T.; Furutani, Y.; Okumura, K.; Kokubo, K.; Sakata, T.; Yasuda, H.; Yakiyama, Y.; Sakurai, H. *Sci. Rep.* **2017**, *7*, 9579.

73. Matsuo, A.; Hasegawa, S.; Takano, S.; Tsukuda, T. *Langmuir* **2020**, *36*, 7844.
74. Hirai, H.; Ito, S.; Takano, S.; Koyasu, K.; Tsukuda, T. *Chem. Sci.* **2020**, *11*, 12233.
75. Tsunoyama, H.; Tsukuda, T. *J. Am. Chem. Soc.* **2009**, *131*, 18216.
76. Ishida, R.; Arii, S.; Kurashige, W.; Yamazoe, S.; Koyasu, K.; Negishi, Y.; Tsukuda, T. *Chin. J. Catal.* **2016**, *37*, 1656.
77. Tsunoyama, H.; Ichikuni, N.; Tsukuda, T. *Langmuir* **2008**, *24*, 11327.
78. Bals, S.; Van Aert, S.; Romero, C. P.; Lauwaet, K.; Van Bael, M. J.; Schoeters, B.; Partoens, B.; Yucelen, E.; Lievens, P.; Van Tendeloo, G. *Nat. Commun.* **2012**, *3*, 897.
79. Lambie, S. G.; Weal, G. R.; Blackmore, C. E.; Palmer, R. E.; Garden, A. L. *Nanoscale Adv.* **2019**, *1*, 2416.
80. Marks, L. D.; Smith, D. J. *Nature* **1983**, *303*, 316.
81. Ajayan, P. M.; Marks, L. D. *Phys. Rev. Lett.* **1988**, *60*, 585.
82. Krakow, W.; Jóse-Yacamán, M.; Aragón, J. L. *Phys. Rev. B: Condens. Matter Mater. Phys.* **1994**, *49*, 10591.
83. Koga, K.; Ikeshoji, T.; Sugawara, K. *Phys. Rev. Lett.* **2004**, *92*, 115507.
84. Iijima, S.; Ichihashi, T. *Phys. Rev. Lett.* **1986**, *56*, 616.

Chapter 2.

Novel Magic Au_{24} Cluster Stabilized by PVP: Selective Formation, Atomic Structure, and Oxidation Catalysis

Hasegawa, S.; Takano, S.; Harano, K.; Tsukuda, T.

JACS Au **2021**, *1*, 660-668.

2.1 Introduction

As described in Chapter 1, Au clusters stabilized by polyvinylpyrrolidone (Au:PVP) with the diameter smaller than ~2 nm show size specific and high catalytic activities for aerobic oxidation reactions that were not scalable with respect to the diameter.[1] On the other hand, gas-phase studies demonstrated that the reactivity of Au cluster anions with molecular oxygen was highly dependent on the number of constituent atoms.[2,3] Thus, it is essential to control the size with atomic precision to take full advantage of size specific catalysis of Au clusters. However, it has been technically challenging to achieve atomically precise size control and determination of atomic structure, since post-synthetic isolation methods and single crystal X-ray diffractometry are not applicable to polymer-stabilized metal clusters.

In this Chapter, I achieved atomically precise synthesis of a novel magic number cluster, Au_{24}:PVP, through the kinetically controlled reduction of a precursor Au complex in the presence of a large amount of PVP. By means of aberration-corrected transmission electron microscopy (ACTEM) with the help of density functional theory (DFT) calculations, I revealed that Au_{24}:PVP was composed of distinctive structural isomers in which all the constituent Au atoms were exposed on the cluster surface and that the atomic structure of Au_{24}:PVP was fluxional due to interconversion between the isomers. X-ray photoelectron spectroscopy (XPS) and Fourier-transform infrared (FT-IR) spectroscopy of adsorbed carbon monoxide indicated that the metal core of Au_{24}:PVP was negatively charged due to the electron transfer from ligating polymers. I studied the catalysis of Au_{24}:PVP using the aerobic oxidation of benzyl alcohol. Clear kinetic isotope effect (KIE) for α-hydrogen and negative reaction constant of the Hammett plot for *p*-substituted benzyl alcohol indicated that the hydride elimination

from α-carbon by Au_{24}:PVP was the rate-determining step of the alcohol oxidation. The apparent activation energy was estimated to be 56 ± 3 kJ mol^{-1} based on the Arrhenius equation. Furthermore, I proposed that the direct hydrogen abstraction by O_2 from alcohol also proceeds, based on the effect of oxygen pressure on the reaction kinetics.

2.2 Methods

2.2.1 Chemicals

All chemicals were commercially available and were used without any further purification. Hydrogen tetrachloroaurate(III) tetrahydrate ($HAuCl_4 \cdot 4H_2O$), sodium borohydride ($NaBH_4$), PVP K-30 (~40 kDa), benzyl alcohol ($C_6H_5CH_2OH$), *p*-methylbenzyl alcohol ($CH_3C_6H_4CH_2OH$), *p*-methoxybenzyl alcohol ($CH_3OC_6H_4CH_2OH$), and potassium carbonate (K_2CO_3) were purchased from Wako Pure Chemical Industries. *p*-(Trifluoromethyl)benzyl alcohol ($CF_3C_6H_4CH_2OH$) and *trans*-2-[3-(4-*tert*-butylphenyl)-2-methyl-2-propenylidene]malononitrile (DCTB) were purchased from Tokyo Chemical Industry. Deuterated benzyl alcohol ($C_6H_5CD_2OH$) was purchased from Sigma-Aldrich. Deionized water (Milli-Q: >18 MΩ cm) was used for all experiments.

2.2.2 Synthesis

Au:PVP were synthesized by microfluidic mixing of two aqueous solutions of a precursor Au complex and reducing agent at 273 K as described in the literature.[4–6] The aqueous solution of $HAuCl_4$ and PVP was mixed with that of $NaBH_4$ and PVP using a micromixer (SIMM-V2, IMM GmbH) at a flow rate of 200 mL h^{-1}. Three samples of Au:PVP (**a**–**c**) were prepared by adjusting the [Au]:[PVP] ratio as listed in **Table 2.1**. The

resulting brown colloidal solution of Au:PVP was collected in an Erlenmeyer flask and stirred for 1 h at 273 K under air. The solution was deionized four times at 273 K by using a centrifugal ultrafiltration concentrator (Vivaspin20, Vivascience) having a membrane filter with a cut-off molecular weight of 10 kDa (for **a**) or 100 kDa (for **b** and **c**) and then lyophilized to obtain the samples as powder. The yields of Au:PVP (**a**–**c**) were calculated to be 79, 73, and 79%, respectively, based on the amount of Au. According to optical spectroscopy and thermogravimetry, the amount of PVP was reduced to ~40 eq (monomer unit of PVP to Au atom) by ultrafiltration. In the catalytic tests, PVP was added to adjust the equivalence to 50.

Table 2.1. Conditions for synthesis of Au:PVP

Sample	Au precursor		Reducing agent		[Au]:[$NaBH_4$]:
	[$HAuCl_4$]/mM	[PVP]/mM[a]	[$NaBH_4$]/mM	[PVP]/mM[a]	[PVP][a]
a	10	200	50	200	1:5:40
b		500		500	1:5:100
c		1000		1000	1:5:200

[a]Concentrations of monomer unit.

2.2.3 Characterization

2.2.3.1 Mass Spectrometry

Matrix-assisted laser desorption/ionization (MALDI) mass spectra were measured by a time-of-flight mass spectrometer (AXIMA-CFR, Shimadzu) with a nitrogen laser (337 nm) in negative mode. DCTB was used as a matrix. The specimens were prepared by drop-casting the methanol solution of Au:PVP and DCTB ([Au] : [DCTB] = 1 : 18) onto a stainless sample plate.

2.2.3.2 Transmission Electron Microscopy

Aberration-corrected transmission electron microscopy (ACTEM) was conducted on an electron microscope (JEM-ARM200F, JEOL) operated at an acceleration voltage of 80 kV, under 1×10^{-5} Pa at 298 K in the specimen column. A series of ACTEM images were continuously acquired with an imaging rate of 25 frames per second (fps) by a CMOS camera (Gatan OneView with in situ option, output image size: 2048 × 2048 pixels operated in the binning 2 mode, pixel resolution: 0.01 nm at ×2000000 magnification). The spherical aberration value, electron dose rate, and defocus value were adjusted to be 1–3 μm, $2.7–5.6 \times 10^6$ e^- nm^{-2} s^{-1}, and approximately –4 nm (underfocus), respectively. In the analysis of recorded images, a bandpass filter was applied using ImageJ software;[7] structures larger than 40 pixels or smaller than 3 pixels were filtered with the tolerance of direction of 5%. The specimens for ACTEM were prepared by drop-casting a methanol dispersion of Au:PVP onto a thin carbon-coated copper grid (SHR-C075, Okenshoji). The histogram of the particle diameter (**Figure 2.2d**) was obtained by measuring the diameters of 388 randomly chosen particles in low magnification (×800000) images.

2.2.3.3 X-ray Absorption Spectroscopy

X-ray absorption spectroscopy (XAS) was carried out in the BL01B1 beamline at Spring-8 of the Japan Synchrotron Radiation Research Institute (JASRI). The incident X-ray beam was monochromatized by a Si(111) double crystal monochromator. All measurements were conducted in transmission mode using ionization chamber at room temperature. Au:PVP were well ground and pressed to form a pellet. The spectral data were analyzed by using a REX2000 program (Rigaku). The k^3-weighted χ spectra in the k range of 3–16.5 $Å^{-1}$ were Fourier-transformed into the r space. The Au–Au and Au–Cl

bonds were considered in the curve-fitting analysis over the *r* range of 1.7–3.0 Å. The phase shifts and back-scattering amplitude functions for Au–Au and Au–Cl bonds were extracted from the simulation results for bulk Au and $AuCl_3$, respectively, calculated by FEFF8 program with Debye-Waller factor of 0.0036 $Å^2$.

2.2.3.4 Fourier-Transform Infrared Spectroscopy

Fourier-transform infrared (FT-IR) spectra of ^{12}CO adsorbed on Au:PVP were measured by using a spectrophotometer (FTIR-4200, JASCO) in transmission mode at a resolution of 2 cm^{-1}. Au:PVP (Au 15 μmol) was dispersed in dichloromethane (3 mL) and the colloidal dispersion was degassed by freeze-pump-thaw (FPT) cycles. After the introduction of CO (1.0 atm), the dispersion was stirred for 50 min and transferred into an IR cell with CaF_2 window.

2.2.3.5 Other Characterization Methods

Optical absorption spectra were measured by a spectrophotometer (V-670, JASCO). Powder X-ray diffraction (PXRD) patterns were obtained using a diffractometer (SmartLab 3, Rigaku) with Cu Kα radiation. X-ray photoelectron spectroscopy (XPS) was conducted by using a PHI-5000 VersaProbe (ULVAC-PHI) instrument with Al Kα X-ray source at an energy resolution of 0.2 eV. Electron binding energy was calibrated by referring to the position of Au $4f_{7/2}$ peak of bulk Au (84.0 eV).

2.2.4 Theoretical Methods

Density functional theory (DFT) calculations on the model structures of Au_{24}, $Au_{24}Cl_4$, and $Au_{24}(CO)_1$ were carried out using Gaussian 09 program.[8] B3LYP hybrid

functional was used for all calculations.[9,10] A double-zeta basis set with scalar relativistic effective core potential (ECP), LANL2DZ, was applied for Au atoms and the 6-31+G(d) basis set was employed for C, O, and Cl atoms. Structures of Au_{24} were obtained by reoptimization of those reported in the literature.[11,12] PVP was not included in the calculations since the impact on the geometrical structure of Au clusters is not significant.[13] Neutral species (Au_{24}, $Au_{24}Cl_4$, and $Au_{24}(CO)_1$) were optimized with the singlet spin state, whereas calcuations of negatively charged clusters, $Au_{24}(CO)_1^-$, were performed with the doublet spin state. The vibrational frequencies were computed for all the optimized structures to ensure that they were located at the local minima of potential energy surface. The relative energy of the clusters includes the zero-point energy. A scaling factor of 0.9702 was applied for the stretching frequencies of CO adsorbed on Au_{24} so that the calculated frequency of isolated CO molecule (2203 cm^{-1}) reproduced the experimental value of free CO in dichloromethane (2136 cm^{-1}).

TEM simulation of DFT-optimized model structures were conducted by using a multislice procedure implemented in a BioNet elbis software;[14] model structures were converted to a series of simulated TEM images with the observation direction varying every 10 degree around the *x* and *y* axes, producing 18 × 36 = 648 images.[15] The defocus value and spherical aberration coefficient (Cs) were set to be –4 nm and –3 μm, respectively, for all simulations. In order to quantify the similarity of the experimental and simulated TEM images, a cross-correlation analysis was carried out.[16,17] The cross-correlation function of two images (a and b), γ(a, b), is defined as follows:

$$\gamma(a,b) = \frac{\sum_{i,j}^{N}\left[I_a(r_{i,j}) - \bar{I_a}\right]\cdot\left[I_b(r_{i,j}) - \bar{I_b}\right]}{\sqrt{\sum_{i,j}^{N}\left[I_a(r_{i,j}) - \bar{I_a}\right]^2}\cdot\sqrt{\sum_{i,j}^{N}\left[I_b(r_{i,j}) - \bar{I_b}\right]^2}} \qquad (2.1)$$

Where I, $r_{i,j}$, and $\bar{I}$ represent the intensity of the image, pixel position, and mean

intensity, respectively. The value of the function is an index of the similarity of two images; γ of 1 or 0 corresponds to a perfect match or no match, respectively. Therefore, the cross-correlation function of the experimental and simulation images was calculated for the efficient screening of the large number of simulation images. Candidate images obtained by the screening were then carefully compared to the observed images.

2.2.5. Catalytic Test

Catalysis of Au:PVP for aerobic oxidation of benzyl alcohol derivatives in water was studied using a temperature-controlled personal organic synthesizer, PPS-2510 (Eyela). The catalytic reaction was initiated by adding the aqueous dispersion (8 mL) of Au:PVP (Au 4 μmol) to the aqueous solution (12 mL) of alcohol (80 μmol) and K_2CO_3 (240 μmol) stirred at 800 rpm. Aliquots (5 mL) were sampled at given reaction time and hydrochloric acid (4M, 150 μL) was added to quench the reaction. Reaction products were extracted by ethyl acetate (1 mL) three times. The extract was dried over Na_2SO_4 and analyzed by a gas chromatograph (GC-2014, Shimadzu) with a flame ionization detector. Rate constants for the oxidation reaction were obtained by linear fitting of the natural logarithm of the substrate concentration using more than 6 points at which the conversion was typically between 10% and 40%. Since the reaction proceeds faster in the initial stage (conversion < 10%), the zero point was excluded for the linear fitting.

2.3 Results and Discussion

2.3.1. Atomically Precise Synthesis of $Au_{24}Cl_x$

In order to examine the effect of the amount of PVP on cluster size, three samples of Au:PVP (**a**–**c**) were prepared at the [Au]:[PVP] ratio of 1:40, 1:100, and 1:200, respectively. The core size distributions of **a**–**c** were evaluated by MALDI mass spectrometry. **Figure 2.1** shows typical negative-mode MALDI mass spectra of **a**–**c** recorded with minimal laser fluence. Sample **a** contained $Au_{34}Cl_x^-$ (x = 0–4) and $Au_{43}Cl_x^-$ (x = 0–4), whereas sample **b** was the mixture of $Au_{24}Cl_x^-$ (x = 0–3), $Au_{33}Cl_x^-$ (x = 0–2), and $Au_{34}Cl_x^-$ (x = 0–3). Most remarkably, the mass spectrum of sample **c** is dominated by the progression of peaks corresponding to $Au_{24}Cl_x^-$ (x = 0–3).

According to classical nucleation theory,[18] selective formation of atomically

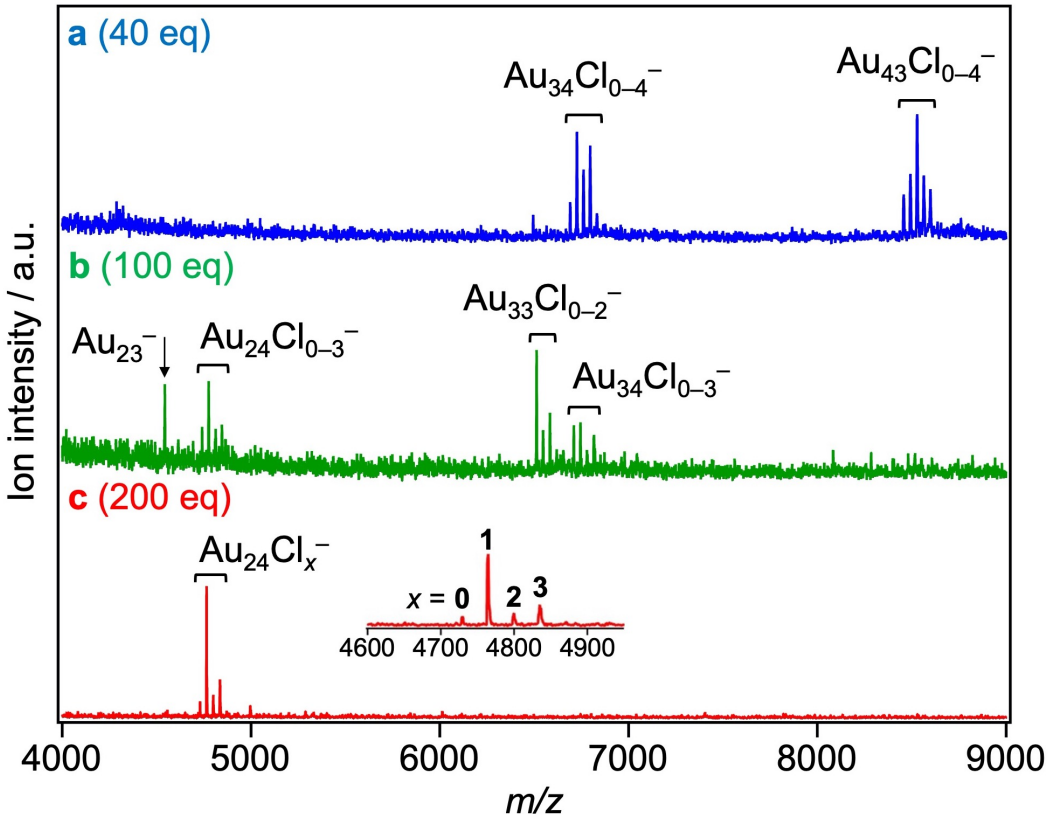

Figure 2.1. Negative-ion MALDI mass spectra of Au:PVP (**a**–**c**).

monodisperse Au_{24} clusters in sample **c** is ascribed to a kinetically controlled nucleation of Au atoms and suppression of the further growth reactions. Such a reaction condition was achieved by rapid and homogeneous reduction of all the precursor complex ($AuCl_4^-$) by the strong reducing agent (BH_4^-) in the micromixer. The trend observed in **Figure 2.1** indicates that PVP also takes an essential role in atomically precise synthesis by retarding the growth process.

The ligation by Cl originating from $AuCl_4^-$ has been frequently observed for small Au clusters such as $Au_{34}Cl_n$, $Au_{43}Cl_n$, $[Au_{11}(PPh_3)_8Cl_2]^+$, and $Au_{55}(PPh_3)_{12}Cl_6$.[6,19,20] According to the elemental analysis of sample **c**, the average number of the Cl ligands on Au_{24} was estimated to be 9.4, suggesting that MALDI process is accompanied by dissociation of the Cl ligands. Observation of the selective dissociation suggests that the Cl ligands are weakly bound to Au_{24} as electron withdrawing ligands as implied by weak magic behavior at x = 1 and 3 in **Figure 2.1c**.

Non-contamination of sample **c** with Au particles larger than 2 nm was confirmed by the following results: (1) absence of localized surface plasmon resonance (LSPR) band at ~520 nm in the UV-Vis absorption spectrum (Figure **2.2a**); (2) observation of a single broad peak at ~40 degree in the PXRD pattern (Figure **2.2b**); (3) small coordination number (CN) of the Au–Au bond (4.2 ± 0.5) obtained by the curve fitting analysis of the Au L_3-edge EXAFS (**Figure 2.2c**, **Table 2.2**); average diameter of Au clusters estimated to be 1.0 ± 0.2 nm by ACTEM (**Figure 2.2d**). I concluded from these results that single-sized Au_{24} cluster was selectively formed in sample **c** with Cl ligands. In the following, I focus on sample **c**, which is hereafter referred to as Au_{24}:PVP.

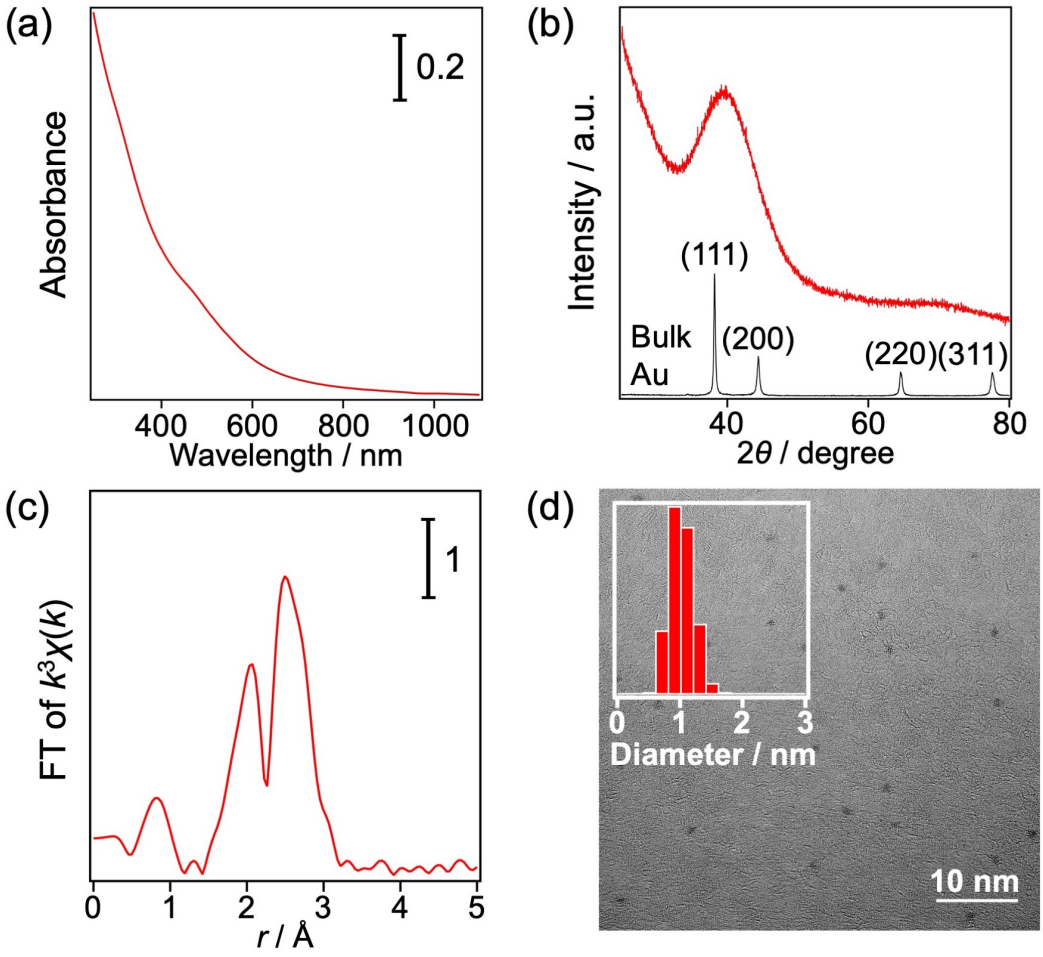

Figure 2.2 (a) Optical absorption spectrum in water ([Au] = 0.2 mM), (b) PXRD pattern, (c) Au L_3-edge FT-EXAFS spectrum, and (d) representative ACTEM image with low magnification (×800000) of Au:PVP (sample **c**). The inset of panel (d) indicates the diameter distribution of 388 randomly chosen particles.

Table 2.2. Structural parameters obtained by curve-fitting analysis of Au L_3-edge EXAFS

Sample	Bond	CN [a]	r / Å [b]	σ^2 / Å^2 [c]	R / % [d]
Au:PVP	Au–Cl	0.7(2)	2.34(2)	0.007(4)	7.4
(sample **c**)	Au–Au	4.2(5)	2.71(1)	0.0086(9)	

[a] Coordination number. [b] Bond length. [c] Debye-Waller factor. [d] R is defined as follows;
$R = (\Sigma(k^3\chi^{data}(k)-k^3\chi^{fit}(k))^2)^{1/2}/(\Sigma(k^3\chi^{data}(k))^2)^{1/2}$

2.3.2. Geometrical Structure of Au_{24}:PVP

It is well known that the magic stability of bare Au clusters is governed by electronic shell closure based on a jellium model.[21] The formation of Au_{34} and Au_{58} clusters in PVP reported in previous studies is explained by the same model.[6,22] In contrast, $Au_{24}Cl_x$ in Au_{24}:PVP corresponds to an unprecedented magic cluster. This result implies that the $Au_{24}Cl_x$ clusters do not have a spherical shape and do not provide spherical effective potential to confine valence electrons. To obtain an insight into the atomic structure of $Au_{24}Cl_x$, I first conducted DFT calculations on Cl-free Au_{24} clusters. **Figure 2.3** shows the DFT-optimized structures of Au_{24} (**1**–**7**) in the order of the relative stability and frontier Kohn-Sham orbitals of **1**–**7** are depicted in **Figure 2.4**. The relative energies (ΔE) and energy gap between highest occupied molecular orbital (HOMO) and the lowest unoccupied molecular orbital (LUMO) are summarized in **Table 2.3**. Interestingly, all the constituent Au atoms of isomers **1**–**6** are located on the surface: **1** and **3** have flat cage structures; **4** and **6** show hollow tubular geometries; and **2** is composed of an Au_4 unit and

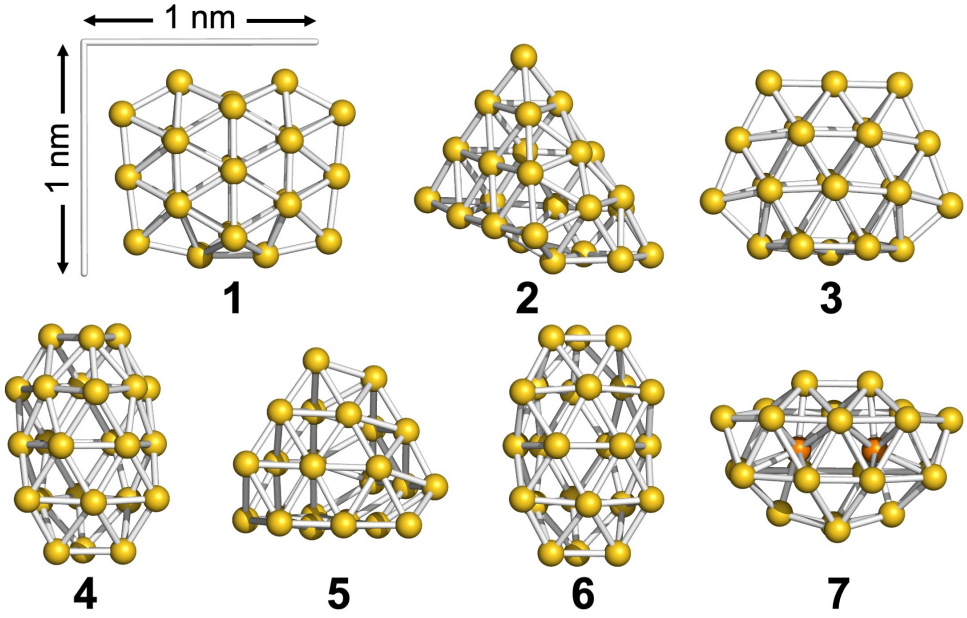

Figure 2.3. DFT-optimized model structures of Au_{24}.

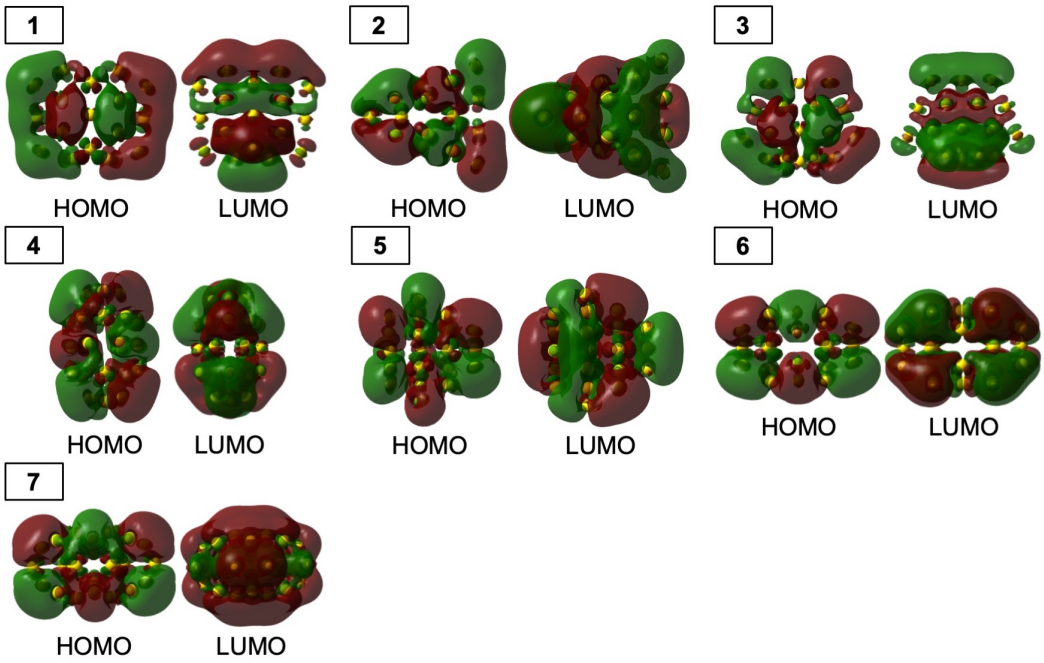

Figure 2.4. Frontier Kohn-Sham orbitals of Au_{24} isomers shown in **Figure 2.3**.

Table 2.3. Relative energies and HOMO-LUMO gaps of structural isomers of Au_{24} and $Au_{24}Cl_4$.

Au_{24}			$Au_{24}Cl_4$		
Isomer	ΔE / eV [a]	HLG / eV [b]	Isomer	ΔE / eV [a]	HLG / eV [b]
1	0	1.56	**1Cl**	0.33	1.10
2	0.02	1.28	**2Cl**	1.05	1.64
3	0.30	1.12	**3Cl**	0.14	1.64
4	0.31	1.60	**4Cl**	0	1.60
5	0.33	1.11	**5Cl**	0.72	1.25
6	0.61	1.29	**6Cl**	0.18	1.40
7	1.64	1.20			

[a]Relative energy. [b]HOMO-LUMO gap.

well known pyramidal magic Au_{20} cluster.[23] In contrast, the least stable isomer **7** has two inner Au atoms encapsulated by the Au_{22} cage. The dimensions of structures **1**–**7** are

consistent with the result of size evaluation by ACTEM (**Figure 2.2d**). The projection of **4** or **6** along the longitudinal axis gave the smallest diameter of ~0.7 nm, whereas that of **1** or **3** from the flattened surface normal gave the largest diameter of ~1.3 nm (**Figure 2.5**). This semiquantitative agreement indicates the validity of the structural models in **Figure 2.3**. These results suggest that various non-crystalline structures such as **1**–**6**, in which all the constituent Au atoms are exposed on the cluster surface, are energetically accessible.

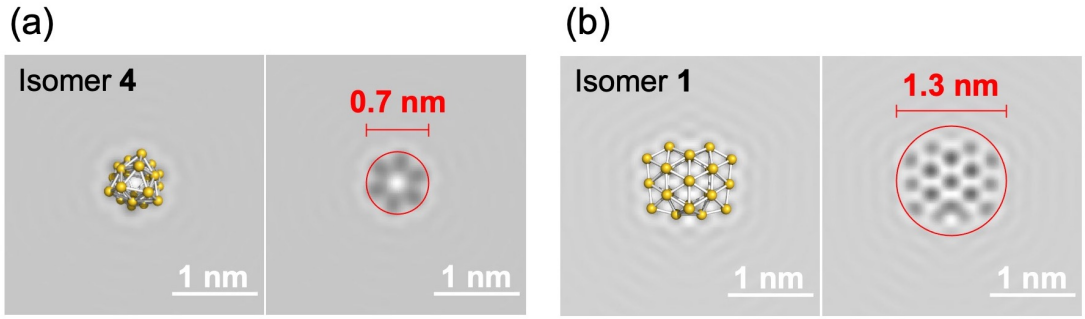

Figure 2.5. Simulated TEM images of Au_{24} showing (a) minimum and (b) maximum diameter.

Then, the effect of Cl ligands on the geometrical structures of Au_{24} was examined by using $Au_{24}Cl_4$ with 20 valence electrons as a model. **Figure 2.6** shows the structural isomers **1Cl**–**6Cl** obtained by optimizing the initial structures in which four Cl ligands are attached to low coordination atoms of low energy isomers **1**–**6** in **Figure 2.3**, respectively. The frontier Kohn-Sham orbitals of **1Cl**–**6Cl** are depicted in **Figure 2.7**. Cl ligation induced the slight distortion of the Au frameworks and as a result the relative stability of the isomers was changed. Nevertheless, it is safe to conclude that the metal core of $Au_{24}Cl_4$ can take structures where all the Au atoms are located on the surface, similarly to the bare clusters. The CN values and average bond length between Au atoms in **1**–**7** and **1Cl**–**6Cl** are summarized in **Table 2.4**. The Au–Au CNs in **1**–**7** (5.1–5.5) and **1Cl**–**6Cl** (4.4–4.8) qualitatively agreed with that (4.2 ± 0.5) obtained by Au L_3-edge

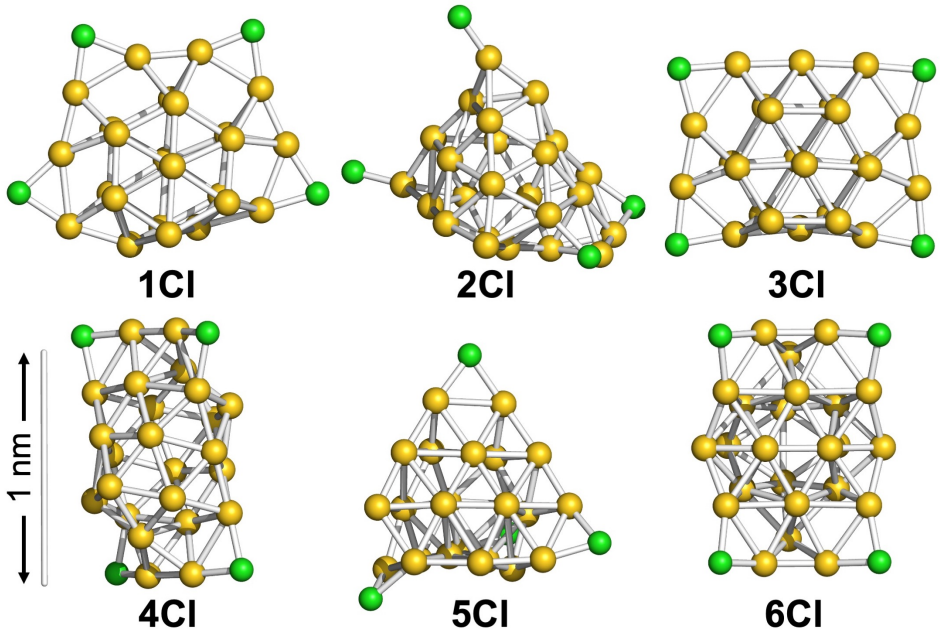

Figure 2.6. DFT-optimized model structures of $Au_{24}Cl_4$.

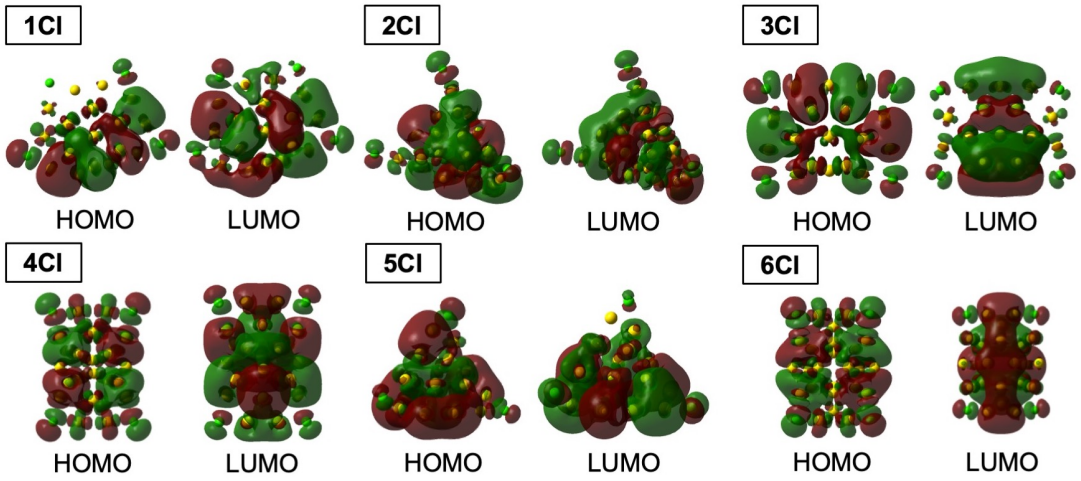

Figure 2.7. Frontier Kohn-Sham orbitals of $Au_{24}Cl_4$ isomers shown in **Figure 2.6**.

EXAFS analysis (**Table 2.2**), while the calculated average bond length of Au–Au bonds in **1**–**7** (2.87–2.90 Å) and **1Cl**–**6Cl** (2.85–2.87 Å) are longer than that (2.71 ± 0.01 Å) experimentally estimated. In the following discussion on the geometrical structures, Cl ligands are not taken into consideration.

Table 2.4. Au–Au coordination numbers (CNs) and average Au–Au bond length (<*r*>) of DFT-optimized Au_{24} in **Figure 2.3** and $Au_{24}Cl_4$ in **Figure 2.5**.

Au_{24}			$Au_{24}Cl_4$		
Isomer	CN [a]	<*r*> / Å [a]	Isomer	CN [a]	<*r*> / Å [a]
1	5.5	2.88	**1Cl**	4.8	2.86
2	5.1	2.88	**2Cl**	4.7	2.85
3	5.5	2.89	**3Cl**	4.7	2.86
4	5.5	2.87	**4Cl**	4.7	2.85
5	5.5	2.90	**5Cl**	4.6	2.87
6	5.5	2.87	**6Cl**	4.4	2.87
7	5.2	2.90			

[a] Pairs of Au atoms with an interatomic distance smaller than 3.05 Å were considered to be bonding.

Theoretical prediction of distinct geometrical structures with similar stability suggests that Au_{24} clusters in PVP are the mixture of structural isomers and/or interconvert among the isomers under ambient temperature. To address this interesting issue, atomic structures of Au_{24}:PVP were probed by ACTEM video imaging at 25 images per second. The ACTEM images of Au_{24}:PVP did not show any signs of atom ejection by electron beam irradiation during continuous observation of several minutes. **Figure 2.8** shows representative ACTEM snapshots of different Au_{24} particles (**#1**–**#7**). The images could not be reproduced by assuming single isomer in **Figure 2.3** but could be by using different isomeric forms of **1**, **2**, **2**, **4**, **5**, **5**, and **7**, respectively. No images could not be assigned to the icosahedral nor face-centered cubic structures observed in the selenolate (RSe)- or thiolate (RS)-protected gold clusters, $Au_{25}(SeR)_{18}$ and $Au_{144}(SR)_{60}$.[24] Furthermore, the images of single Au_{24} particle (**#8**) fluctuated every 0.08–0.4 s during

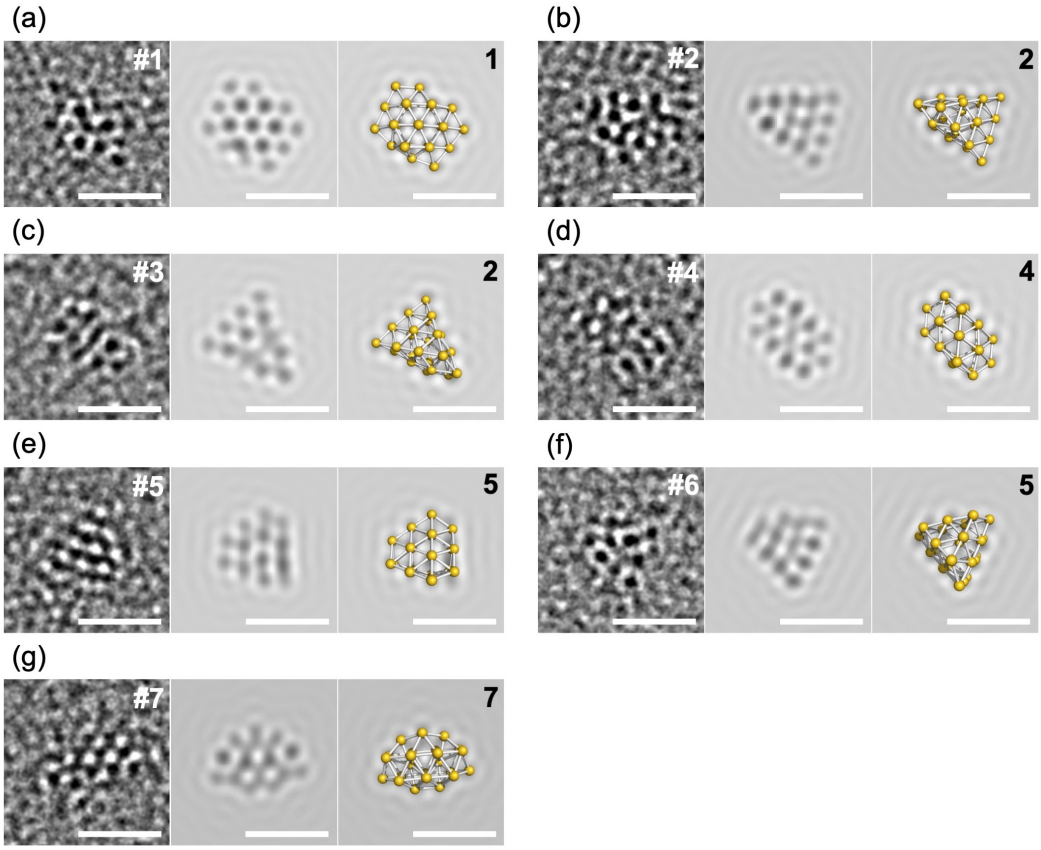

Figure 2.8. Representative ACTEM snapshots of different particles of Au_{24}:PVP (**#1**–**#7**), assigned simulated images, and corresponding Au_{24} isomers in **Figure 2.3**. Scale bars correspond to 1 nm.

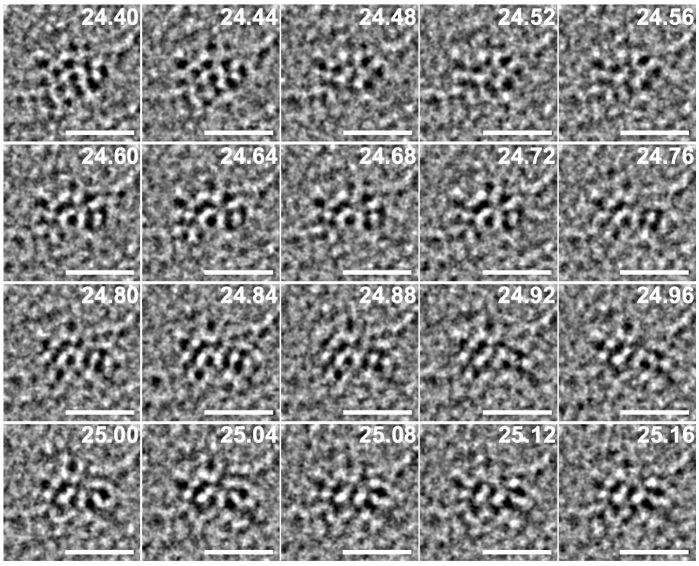

Figure 2.9. ACTEM image sequence of single particle of Au_{24}:PVP (**#8**). The value in the upper right of each image is the time in seconds from the beginning of the recording. Scale bars correspond to 1 nm.

the observation, as shown in **Figure 2.9**. ACTEM snapshots of particle **#8** at different times (t_1–t_4) in **Figure 2.10** could not be explained by the simple rotation of single isomer. Comparison with a set of images simulated by systematically changing the projection directions and structural isomers revealed that the temporal change of the ACTEM image of particle **#8** was derived from the structural isomerization; the images of **Figures 2.10a–d** are assigned to the distinctive isomers **5**, **2**, **6**, and **6** (**Figures 2.10i–l**), respectively. Thus, I revealed the dynamic nature of Au_{24} core by direct observation of the structural isomerization. The coexistence of isomers with hollow tubular structures has also been proposed for the bare cluster anion, Au_{24}^-, in gas phase.[25]

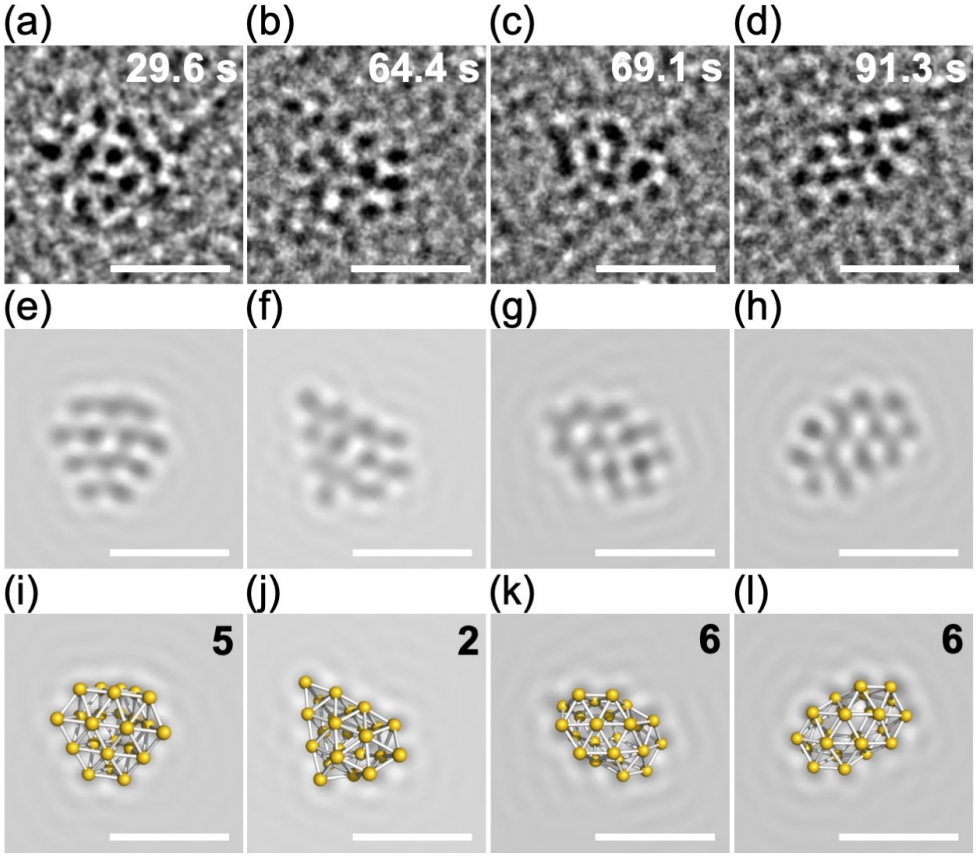

Figure 2.10. (a–d) Representative ACTEM snapshots of single Au_{24} particle (**#8**) at different times from the beginning of the video recording (t_1: 29.6 s, t_2: 64.4 s, t_3: 69.1 s, t_4: 91.3 s), (e–h) assigned simulation images, and (i–l) corresponding structural isomers of Au_{24} in **Figure 2.3**. Scale bars correspond to 1 nm.

At present, the selective formation of Au_{24}:PVP could not be explained in terms of the electronic nor geometrical shell closure. I speculate that the cavity volume created by the multiple PVP chains determines the preferable size of Au clusters to be stabilized.

2.3.3. Electronic Structure of Au_{24}:PVP

Although $Au_{24}Cl_x$ was synthesized with atomic precision, the optical absorption spectrum in **Figure 2.2a** shows a featureless profile. This phenomenon was ascribed to the heterogeneity of the atomic structures of clusters, considering that HOMO-LUMO gaps of stable isomers (**1**–**6**) varied significantly (1.1–1.6 eV) depending on the geometrical structures (**Table 2.3**).

The electronic structure of Au_{24}:PVP was further characterized by XPS and FT-IR

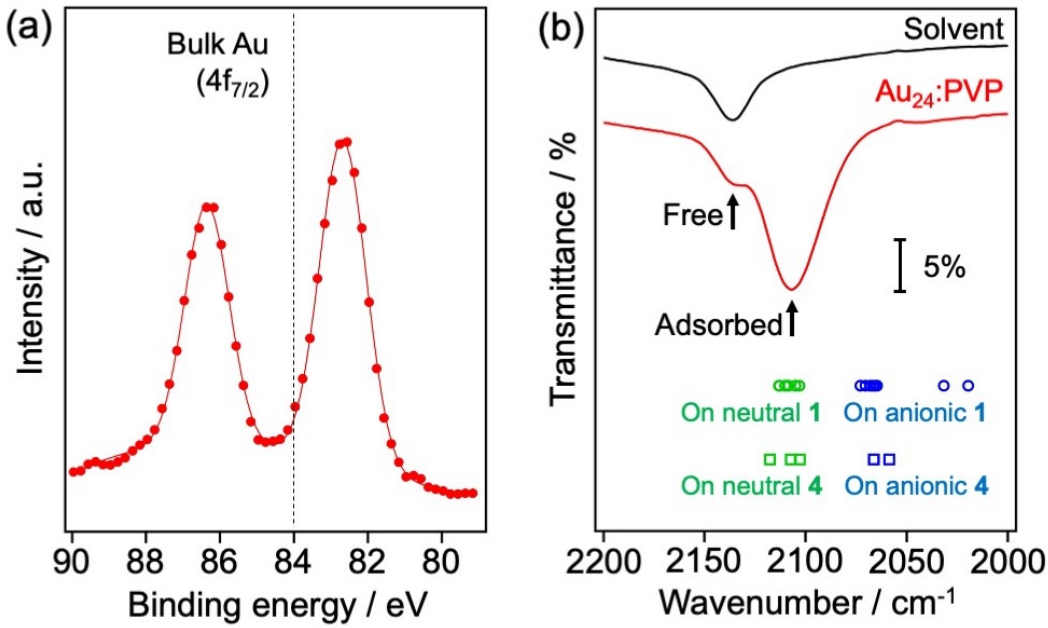

Figure 2.11. (a) XP spectrum of Au_{24}:PVP. (b) FT-IR spectra of ^{12}CO-saturated dichloromethane (black), ^{12}CO-saturated colloidal solution of Au_{24}:PVP (red), and calculated stretching frequencies of ^{12}CO adsorbed on different adsorption sites of isomer **1** (circle) or **4** (square) in **Figure 2.3** with a total charge of 0 (green) or –1 (blue). Details are shown in **Table 2.5**.

spectroscopy using ^{12}CO as a probe with the help of DFT calculations. The XP spectrum of Au_{24}:PVP shows an Au $4f_{7/2}$ peak at 82.7 eV (**Figure 2.11a**), which is significantly red-shifted from that of bulk Au at 84.0 eV. This observation indicates that $Au_{24}Cl_x$ is negatively charged due to the electron transfer from the side chain of PVP,[5] although DFT calculations indicated that the Cl ligands of $Au_{24}Cl_4$ withdrew the electronic charge from Au_{24}: the natural charge of the Cl ligand was calculated to be ~ –0.5.

It is known that the stretching frequency of the adsorbed carbon monoxide reflects the electron density of the adsorption site of Au clusters.[26-29] The FT-IR spectrum of CO-

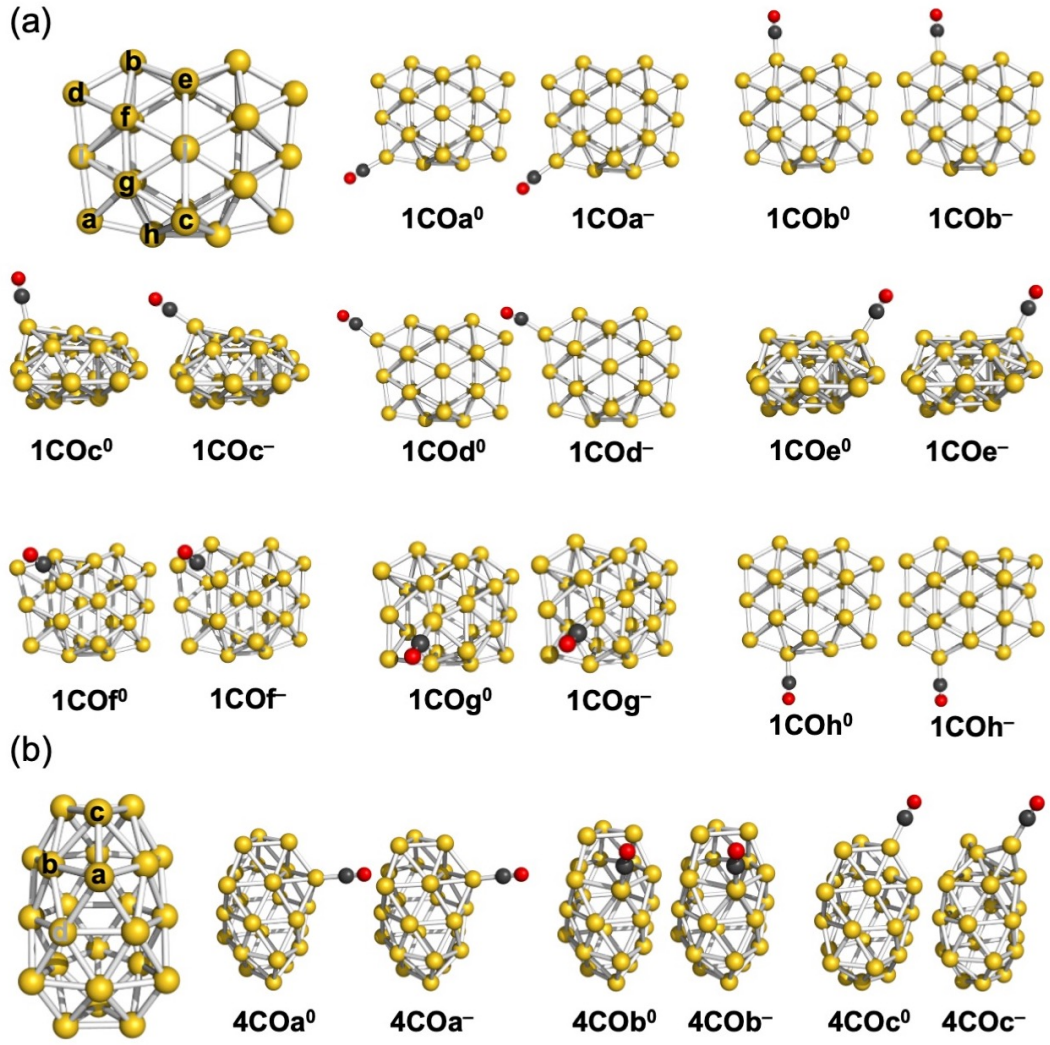

Figure 2.12. Adsorption sites and CO-adsorbed structures of isomers (a) **1** and (b) **4** in **Figure 2.3**. Gray sites were inactive for adsorption.

saturated colloidal solution of Au_{24}:PVP shows a broad peak of CO adsorbed on $Au_{24}Cl_x$ at 2106 cm^{-1} in addition to that of free CO at 2136 cm^{-1} (**Figure 2.11b**). The red-shift of the stretching frequency is attributed to the π back donation from the electron rich Au atoms of $Au_{24}Cl_x$ to adsorbed CO.[29] To obtain deeper insights into the geometrical and electronic structures of Au_{24}:PVP, CO-adsorbed Au clusters were theoretically studied employing two Au_{24} isomers (**1** and **4**) with a charge state of 0 and –1. DFT-optimized structures of $Au_{24}(CO)_1$ are illustrated in **Figure 2.12**; isomers **1COa^0**–**1COh^0** and **1COa$^-$**–**1COh$^-$** correspond to the neutral and anionic **1** adsorbing CO at different sites (**a**–**h**), respectively, whereas **4COa^0**–**4COc^0** and **4COa$^-$**–**4COc$^-$** were the adducts between **4** and CO with the total charge of 0 and –1, respectively. The adsorption energies

Table 2.5. Adsorption energies (E_{ads}) and stretching frequencies of CO (ν_{CO}) at different adsorption sites of Au_{24} isomer **1** and **4** in **Figure 2.3**.

Isomer	E_{ads} / eV	ν_{CO} / cm^{-1}	Isomer	E_{ads} / eV	ν_{CO} / cm^{-1}
1COa^0	0.32	2109	**1COa$^-$**	0.22	2066
1COb^0	0.28	2109	**1COb$^-$**	0.10	2020
1COc^0	0.27	2113	**1COc$^-$**	0.29	2065
1COd^0	0.23	2103	**1COd$^-$**	0.14	2032
1COe^0	0.23	2110	**1COe$^-$**	0.21	2070
1COf^0	0.17	2108	**1COf$^-$**	0.11	2073
1COg^0	0.13	2113	**1COg$^-$**	0.16	2067
1COh^0	0.11	2105	**1COh$^-$**	0.17	2068
4COa^0	0.42	2103	**4COa$^-$**	0.31	2066
4COb^0	0.23	2118	**4COb$^-$**	0.28	2066
4COc^0	0.19	2107	**4COc$^-$**	0.38	2059

and stretching frequencies of adsorbed CO are summarized in **Table 2.5**. The adsorption energies are in the range of 0.1–0.4 eV regardless of the core structures, total charges, and adsorption sites. The CO stretching frequencies on neutral **1** and **4** (green plots in **Figure 2.11b**) varied only slightly (<20 cm^{-1}) depending on the adsorption sites and can explain the observed spectrum. In contrast, the CO stretching frequencies on negatively charged **1** and **4** (blue plots in **Figure 2.11b**) are considerably redshifted from those on neutral clusters. Although the structure of $Au_{24}Cl_x$ core and adsorption site of CO could not be identified from these results, they suggest that the negative charge on the $Au_{24}Cl_x$ core is smaller than 1e as a result of the competition between the electron-withdrawing nature of Cl ligands and electron-donating nature of PVP.

2.3.4. Aerobic Oxidation Catalysis of Au_{24}:PVP

The reaction mechanism of the aerobic oxidation of benzyl alcohol catalyzed by Au_{24}:PVP was studied by analyzing the substituent effect and kinetic isotope effect on reaction rate constants. Kinetic measurements were conducted for the oxidation of *p*-substituted benzyl alcohols X-$C_6H_4CH_2OH$ (X = OCH_3, CH_3, H, CF_3) (**Scheme 2.1**). The selectivity for aldehydes and carboxylic acids was affected by the substituent group X (**Figure 2.13**). The pseudo-first-order rate constant was estimated from the time course of the alcohol concentration. The effect of X on the rate constant was analyzed by

Scheme 2.1. Aerobic oxidation of *p*-substituted benzyl alcohol X–$C_6H_4CH_2OH$ (X = OCH_3, CH_3, H, CF_3) catalyzed by Au_{24}:PVP.

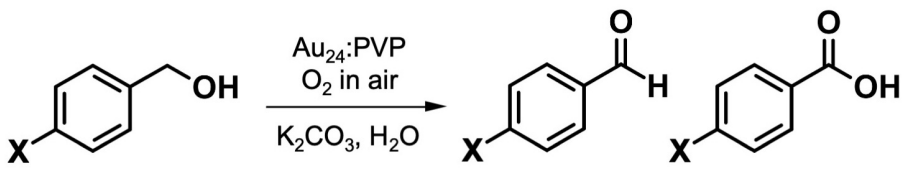

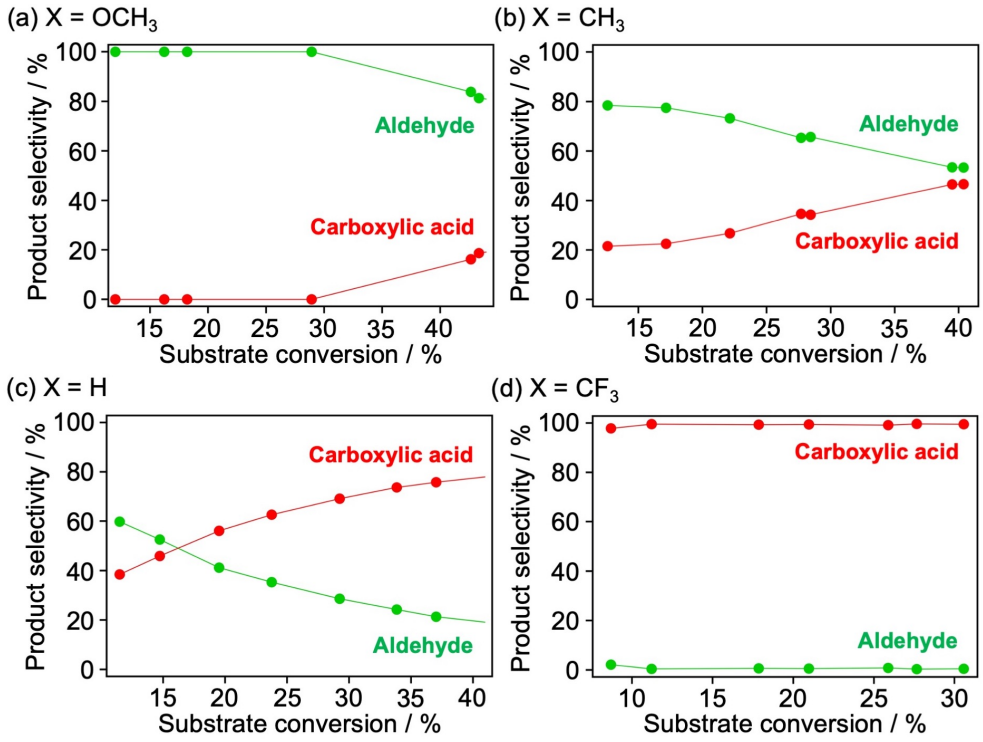

Figure 2.13. Product selectivity of the aerobic oxidation of *p*-substituted benzyl alcohol. Reaction conditions: substrate 80 μmol; Au_{24}:PVP 5 atom%; K_2CO_3 300 mol%; H_2O 20 mL; air; 303 K (unless specified).

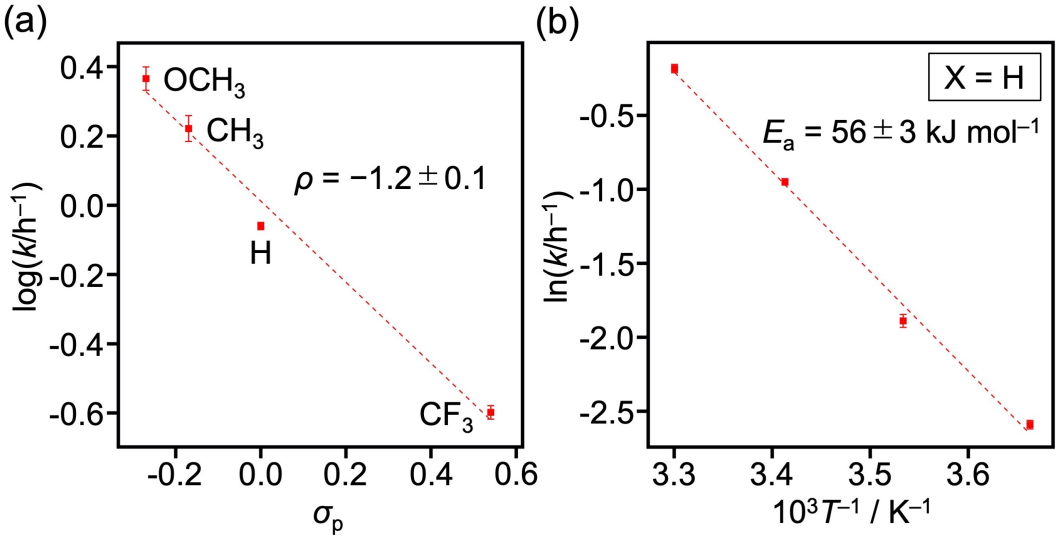

Figure 2.14. (a) Hammett plot for the aerobic oxidation of *p*-substituted benzyl alcohol catalyzed by Au_{24}:PVP (**Scheme 2.1**).[30] (b) Arrhenius plot for the benzyl alcohol oxidation (X = H). Reaction conditions were the same as those described in **Figure 2.13**.

Hammett plot (**Figure 2.14a**) and negative reaction constant ($\rho = -1.2 \pm 0.2$) was obtained.

This result indicated that the α-carbon of alcohol had cationic characteristics at the transition state of the rate-determining step. Furthermore, a large kinetic isotope effect (KIE = k_H/k_D) of 4.1 was observed for α-deuterated benzyl alcohol ($C_6H_5CD_2OH$). Therefore, it was concluded that the C–H bond cleavage at the α-position was rate-determining step and that the H atom was abstracted as a hydride. The apparent activation energy for the oxidation of pristine benzyl alcohol (X = H) was evaluated to be 56 ± 3 kJ mol^{-1} from the Arrhenius plot (**Figure 2.14b**).

Importantly, it was confirmed by MALDI mass spectrometry, optical absorption spectroscopy, and Au L_3-edge EXAFS that the core size of Au_{24}:PVP was retained during the catalytic reactions (**Figures 2.15** and **16**, and **Table 2.6**). In contrast, MALDI mass

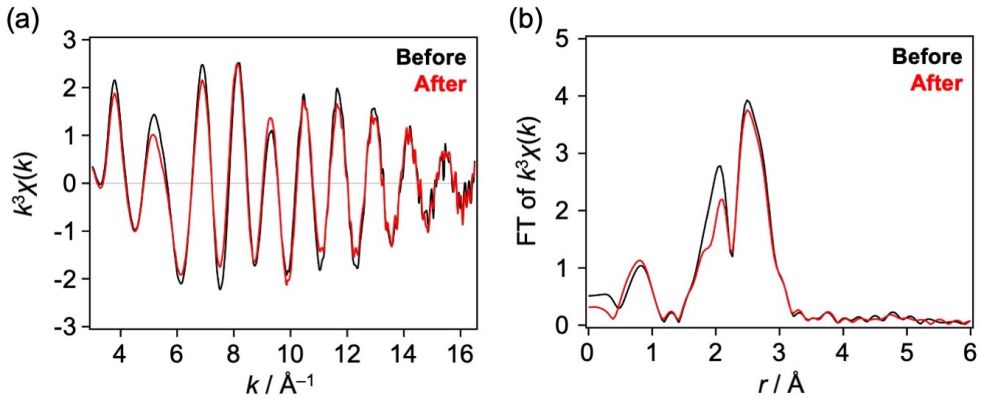

Figure 2.15. Au L_3-edge (a) EXAFS and (b) FT-EXAFS spectra of Au_{24}:PVP before (black) and after (red) the catalytic oxidation of benzyl alcohol.

Table 2.6. Structural parameters of Au_{24}:PVP before and after benzyl alcohol oxidation obtained by curve fitting analysis of Au L_3-edge EXAFS data shown in **Figure 2.16**.

Sample	Bond	CN [a]	r / Å [b]	σ^2 / Å^2 [c]	R / % [d]
Au_{24}:PVP (before)	Au–Cl	0.7(2)	2.34(2)	0.007(4)	7.4
	Au–Au	4.2(5)	2.71(1)	0.0086(9)	
Au_{24}:PVP (after)	Au–Au	4.7(4)	2.72(1)	0.0094(8)	15.0

[a] Coordination number. [b] Bond length. [c] Debye-Waller factor. [d] R is defined as follows;
$R = (\Sigma(k^3\chi^{data}(k)-k^3\chi^{fit}(k))^2)^{1/2}/(\Sigma(k^3\chi^{data}(k))^2)^{1/2}$

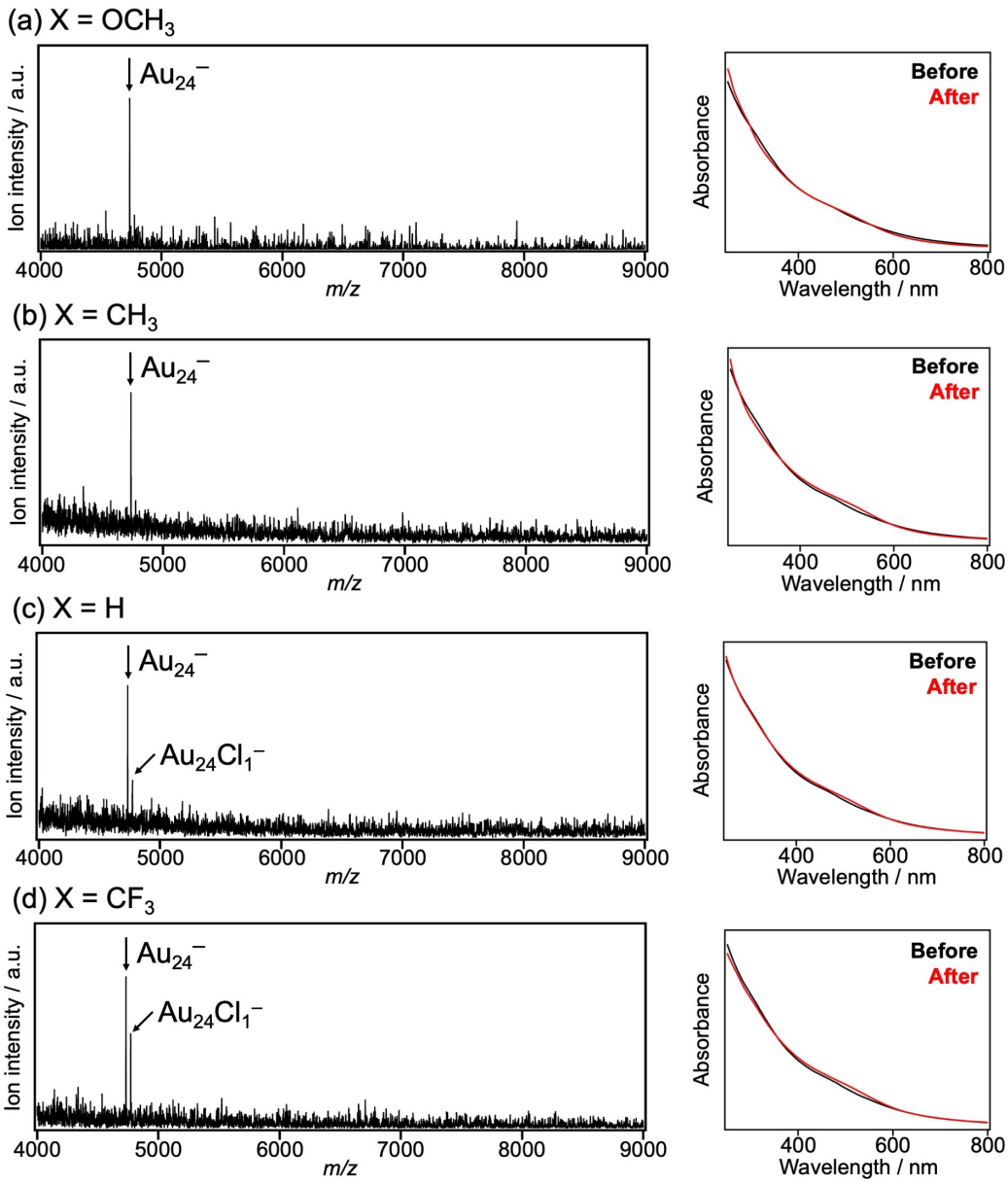

Figure 2.16. MALDI mass spectra and optical absorption spectra of Au_{24}:PVP after catalytic oxidation of *p*-substituted benzyl alcohol at 303 K.

spectrometry and Au L_3-edge EXAFS suggested the loss of Cl ligands during the reactions. These results indicate that the observed catalysis is intrinsic to Au_{24} core and not affected by the Cl ligands. The negligible effect of Cl on the catalysis was supported by the fact that different batches of Au_{24}:PVP containing a different amount of Cl showed similar catalytic activities. Furthermore, it was reported that the Cl ligands of PVP-

stabilized $Au_{34}Cl_n$ and $Au_{43}Cl_n$ clusters were easily released during the alcohol oxidation and did not affect the catalytic activity.[6]

Two different mechanisms have been proposed for aerobic oxidation of alcohols in which O_2 plays different roles. Our group has proposed that O_2 is adsorbed and activated by electron transfer from negatively charged Au:PVP based on the correlation between the electron affinities of bare Au clusters (Au_n) and reactivities of corresponding cluster anions (Au_n^-) toward O_2 in gas phase.[5] In this reaction mechanism, the resulting superoxo-like species abstracts the hydrogen atom from the α-carbon of co-adsorbed alkoxide (**Scheme 2.2a**).[31] A similar mechanism has been proposed by Ebitani for the alcohol oxidation catalyzed by hydrotalcite-supported metal (AuPd, AuPt, or Pt) NPs co-stabilized by polymers such as PVP and starch.[32–34] The other mechanism, proposed by Kobayashi, Chechik, and co-workers is based on the observation of an Au–H intermediate by electron paramagnetic resonance spectroscopy during the alcohol oxidation on Au NPs stabilized by styrene-based copolymers (Au:PS): hydride is directly transferred to the surface of Au:PS and the adsorbed hydride is removed by O_2 (**Scheme 2.2b**).[35] This hydride elimination mechanism has been accepted for the alcohol oxidation catalyzed by Au NPs supported on metal oxides such as TiO_2, CeO_2, and Al_2O_3.[36–41] A similar

Scheme 2.2. Previously proposed reaction mechanisms of alcohol oxidation catalyzed by (a) Au:PVP and (b) Au:PS.

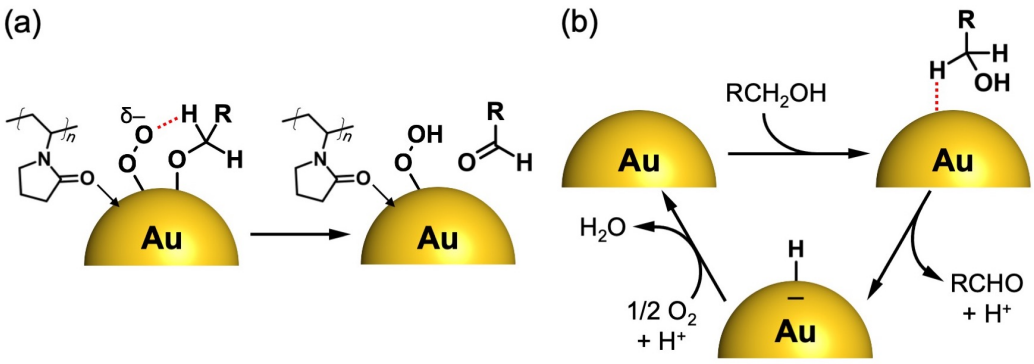

mechanism was proposed for the hydroxyapatite-supported Pd catalyst by Kaneda.[42]

The reaction constant of Hammett plot for Au_{24}:PVP catalyst (**Figure 2.14a**, –1.2 ± 0.2) is comparable to those reported for Au NPs supported on metal oxides (–0.2 to –1.4) where alcohol oxidation proceeds by the hydride elimination mechanism (**Scheme 2.2b**).[36,37,39,41] This fact supports the hydride elimination mechanism for the alcohol oxidation by Au_{24}:PVP. To obtain further insight into the reaction mechanism by Au_{24}, the effect of O_2 pressure was studied. The time course of the alcohol oxidation under atmospheric pressure of O_2 (**Figure 2.17a**) showed two characteristic behaviors: (1) for t > 0.05 h (t: reaction time), the rate constant under pure O_2 (1.0 atm O_2, 1.18 h^{-1}) was larger than that under air (0.21 atm O_2, 0.87 h^{-1}), although the rate constants were not proportional to the oxygen pressure; (2) the rate constant at the initial stage (t < 0.05 h) was apparently larger than that for t > 0.05 h. The former can be understood by the hydride elimination mechanism with the assumption that the removal of surface hydride by O_2 is

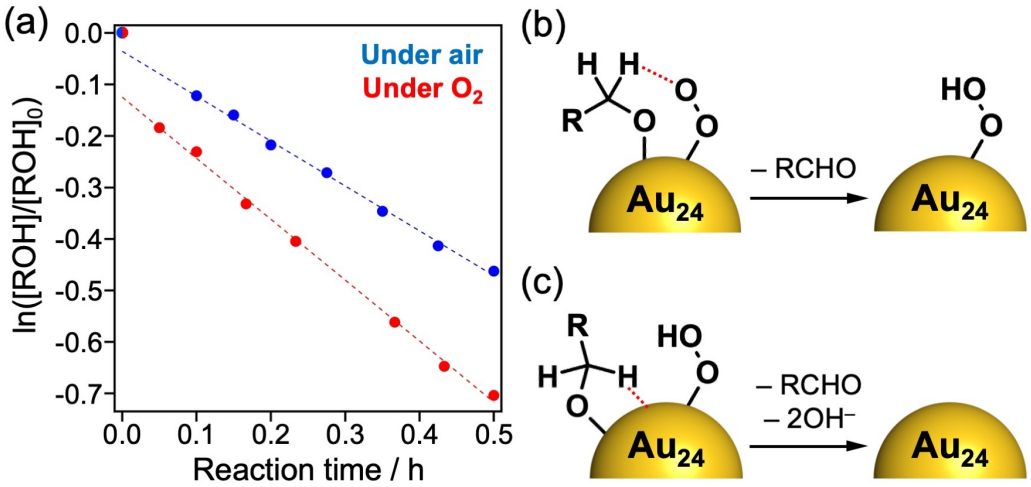

Figure 2.17. (a) Natural logarithm of substrate concentration (normalized by initial concentration) during the catalytic oxidation of benzyl alcohol under air (blue, O_2: 0.21 atm) or pure O_2 (red, O_2: 1.0 atm). Reaction conditions other than O_2 pressure were the same as those for **Figure 2.13**. Two alcohol oxidation pathways on Au_{24}:PVP: (b) hydrogen abstraction by adsorbed O_2 and (c) hydride elimination by Au_{24} surface.

not much faster than the hydride transfer from α-carbon to Au_{24}. However, it was difficult to explain the latter only by hydride elimination mechanism. I propose that hydrogen abstraction by O_2 (**Figure 2.17b**) also proceeds in addition to the hydride elimination by Au_{24} (**Figure 2.17c**). Involvement of the two mechanisms for alcohol oxidation was supported by a recent theoretical study on the oxidation of *p*-hydroxybenzyl alcohol catalyzed by a model cluster $Au_{38}L_3$ (L = 2-pyrrolidone) reported by Okumura.[43] It was concluded that the most plausible catalytic cycle consisted of two consecutive steps: hydrogen abstraction by O_2 (step 1) and hydride elimination by Au_{38} (step 2):

Step 1: $ArCH_2O^- + O_2 + [Au_{38}L_3] \rightarrow ArCHO + [(HOO)Au_{38}L_3]^-$

Step 2: $ArCH_2O^- + [(HOO)Au_{38}L_3]^- \rightarrow ArCHO + 2OH^- + [Au_{38}L_3]$

The cooperation of two oxidation pathways was attributed to the order of the reactivities of oxidants: (O_2 on Au_{38}) > (Au_{38} surface) > (HOO on Au_{38}).

2.4 Summary

In summary, I successfully synthesized a novel magic number cluster, Au_{24}:PVP, by homogenizing the nucleation process using a micromixer and suppressing the growth step by a large amount of PVP. Polydisperse and dynamic nature of the atomic structure of Au_{24}:PVP was revealed by ACTEM video imaging with the help of TEM simulation using theoretically optimized model structures. DFT calculations suggested the disordered structures with all constituent Au atoms located on the surface. Since the magic stability of Au_{24}:PVP could not be explained by electronic nor geometrical shell closure, I speculate that the formation of an unprecedented magic number is associated with the cavity size created by assemblies of PVP in which Au clusters can be confined. Au_{24}:PVP catalyzed the aerobic oxidation of benzyl alcohol derivatives while retaining the cluster

size. I revealed by kinetic studies that the hydride elimination from the benzylic carbon by Au_{24} surface is the rate-determining step with an apparent activation energy of 56 ± 3 kJ mol^{-1}. It was also suggested from the effect of O_2 pressure on the reaction kinetics that the hydrogen abstraction by the adsorbed O_2 proceeds as well. I propose that alcohol oxidation is initiated by the hydrogen abstraction by O_2, followed by the rate-determining hydride elimination by Au_{24}.

References

1. Yamazoe, S.; Koyasu, K.; Tsukuda, T. *Acc. Chem. Res.* **2014**, *47*, 816.
2. Wallace, W. T.; Whetten, R. L. *J. Am. Chem. Soc.* **2002**, *124*, 7499.
3. Pal, R.; Wang, L.-M.; Pei, Y.; Wang, L. S.; Zeng, X. C. *J. Am. Chem. Soc.* **2012**, *134*, 9438.
4. Tsunoyama, H.; Ichikuni, N.; Tsukuda, T. *Langmuir* **2008**, *24*, 11327.
5. Tsunoyama, H.; Ichikuni, N.; Sakurai, H.; Tsukuda, T. *J. Am. Chem. Soc*. **2009**, *131*, 7086.
6. Ishida, R.; Arii, S.; Kurashige, W.; Yamazoe, S.; Koyasu, K.; Negishi, Y.; Tsukuda, T. *Chin. J. Catal.* **2016**, *37*, 1656.
7. Schneider, C.; Rasband, W.; Eliceiri, K. *Nat. Methods* **2012**, *9*, 671.
8. Frisch, M. J.; Trucks, G. W.; Schlegel, H. B.; Scuseria, G. E.; Robb, M. A.; Cheeseman, J. R.; Scalmani, G.; Barone, V.; Mennucci, B.; Petersson, G. A.; Nakatsuji, H.; Caricato, M.; Li, X.; Hratchian, H. P.; Izmaylov, A. F.; Bloino, J.; Zheng, G.; Sonnenberg, J. L.; Hada, M.; Ehara, M.; Toyota, K.; Fukuda, R.; Hasegawa, J.; Ishida, M.; Nakajima, T.; Honda, Y.; Kitao, O.; Nakai, H.; Vreven, T.; Montgomery, J. A., Jr.; Peralta, J. E.; Ogliaro, F.; Bearpark, M.; Heyd, J. J.; Brothers, E.; Kudin, K. N.; Staroverov, V. N.; Keith, T.; Kobayashi, R.; Normand, J.; Raghavachari, K.; Rendell, A.; Burant, J. C.; Iyengar, S. S.; Tomasi, J.; Cossi, M.; Rega, N.; Millam, J. M.; Klene, M.; Knox, J. E.; Cross, J. B.; Bakken, V.; Adamo, C.; Jaramillo, J.; Gomperts, R.; Stratmann, R. E.; Yazyev, O.; Austin, A. J.; Cammi, R.; Pomelli, C.; Ochterski, J. W.; Martin, R. L.; Morokuma, K.; Zakrzewski, V. G.; Voth, G. A.; Salvador, P.; Dannenberg, J. J.; Dapprich, S.; Daniels, A. D.; Farkas, O.; Foresman, J. B.; Ortiz, J. V.; Cioslowski, J.; Fox, D. J. Gaussian 09; Gaussian, Inc.: Wallingford CT, 2009.
9. Lee, C.; Yang, W.; Parr, R. G. *Phys. Rev. B* **1988**, *37*, 785.
10. Becke, A. D. *J. Chem. Phys.* **1993**, *98*, 5648
11. Luo, C.; Fa, W.; Dong, J. *J. Chem. Phys.* **2006**, *125*, 084707.
12. Nhat, P. V.; Si, N. T.; Nguyen, M. T. *J. Phys. Chem. A* **2020**, *124*, 1289.
13. Matsuo, A.; Hasegawa, S.; Takano, S.; Tsukuda, T. *Langmuir* **2020**, *36*, 7844.
14. Hosokawa, F.; Shinkawa, T.; Arai, Y.; Sannomiya, T. *Ultramicroscopy* **2015**, *158*, 56.
15. Kamei, K.; Shimizu, T.; Harano, K.; Nakamura, E. *Bull. Chem. Soc. Jpn.* **2020**, *93*, 1603.
16. Gorgoll, R. M.; Yücelen, E.; Kumamoto, A.; Shibata, N.; Harano, K.; Nakamura, E. *J. Am. Chem. Soc.* **2015**, *137*, 3474.

17. Du. K.; Hochmeister, K. v.; Phillipp, F. *Ultramicroscopy* **2007**, *107*, 281.
18. La Mer, V. K. *Ind. Eng. Chem.***1952**, *44*, 1270.
19. Schmid, G. *Chem. Soc. Rev*. **2008**, *37*, 1909.
20. McKenzie, L. C.; Zaikova, T. O.; Hutchison, J. E. *J. Am. Chem. Soc*. **2014**, *136*, 13426.
21. de Heer, W. A. *Rev. Mod. Phys*. **1993**, *65*, 611.
22. Tsunoyama, H.; Tsukuda, T. *J. Am. Chem. Soc.* **2009**, *131*, 18216.
23. Li, J.; Li, X.; Zhai, H.-J.; Wang, L. S. *Science*. **2003**, *299*, 864.
24. Takahata, R.; Yamazoe, S.; Maehara, Y.; Yamazaki, K.; Takano, S.; Kurashige, W.; Negishi, Y.; Gohara, K.; Tsukuda, T. *J. Phys. Chem. C* **2020**, *124*, 6907.
25. Khetrapal, N. S.; Bulusu, S. S.; Zeng, X. C. *J. Phys. Chem. A* **2017**, *121*, 2466.
26. Yoon. B.; Häkkinen, H.; Landman, U.; Wörz, A. S.; Antonietti, J.-M.; Abbet, S.; Judai, K.; Heiz, U. *Science* **2005**, *307*, 403.
27. Sterrer, M.; Yulikov, M.; Fischbach, E.; Heyde, M.; Rust, H.-P.; Pacchioni, G.; Risse, T.; Freund, H.-J. *Angew. Chem., Int. Ed.* **2006**, *45*, 2630.
28. Fielicke, A.; von Helden, G.; Meijier, G.; Pedersen, D. B.; Simard, B.; Rayner, D. M. *J. Am. Chem. Soc.* **2005**, *127*, 8416.
29. Chen, M.; Goodman, D. W. *Acc. Chem. Res.* **2006**, *39*, 739.
30. Hansch, C.; Leo, A.; Taft, R. W. A. *Chem. Rev.* **1991**, *91*, 165.
31. Tsukuda, T.; Tsunoyama, H.; Sakurai, H. *Chem. Asian J.* **2011**, *6*, 736.
32. Nishimura, S.; Yakita, Y.; Katayama, M.; Higashimine, K.; Ebitani, K. *Catal. Sci. Technol*. **2013**, *3*, 351.
33. Tongsakul, D.; Nishimura, S.; Ebitani, K. *ACS Catal*. **2013**, *3*, 2199.
34. Tongsakul, D.; Nishimura, S.; Ebitani, K. *J. Phys. Chem. C* **2014**, *118*, 11723.
35. Conte, M.; Miyamura, H.; Kobayashi, S.; Chechik, V. *J. Am. Chem. Soc*. **2009**, *131*, 7189.
36. Abad, A.; Corma, A.; García, H. *Chem. Eur. J*. **2008**, *14*, 212.
37. Fristrup, P.; Johansen, L. B.; Christensen, C. H. *Catal. Lett*. **2008**, *120*, 184.
38. Zope, B. N.; Hibbitts, D. D.; Neurock, M.; Davis, R. J. *Science* **2010**, *330*, 74.
39. Kumar, G.; Tibbitts, L.; Newell, J.; Panthi, B.; Mukhopadhyay, A.; Rioux, R. M.; Pursell, C. J.; Janik, M.; Chandler, B. D. *Nat. Chem*. **2018**, *10,* 268.
40. Muñoz-Santiburcio, D.; Camellone, M. F.; Marx, D. *Angew. Chem., Int. Ed.* **2018**, *57*, 3327.
41. Mahdavi-Shakib, A.; Sempel, J.; Babb, L.; Oza, A.; Hoffman, M.; Whittaker, T. N.; Chandler, B. D.; Austin, R. N. *ACS Catal*. **2020**, *10*, 10207.

42. Mori, K.; Hara, T.; Mizugaki, T.; Ebitani, K.; Kaneda, K. *J. Am. Chem. Soc.* **2004**, *126*, 10657.
43. Ato. Y.; Hayashi, A.; Koga, H.; Kawakami, T.; Yamanaka, S.; Okumura, M. *Chem. Phys. Lett.* **2019**, *724*, 115.

Chapter 3.

Single Pd Atom Doping on Au_{24} Cluster Stabilized by PVP: Synthesis, Structural Analysis, and Catalysis

第３章

本章については、５年以内に

雑誌等で刊行予定のため、非公開

Chapter 4.

Selective Synthesis, Atomic Structure, and Size-Specific Oxidation Catalysis of Au_{38} Cluster Stabilized by PVP

第４章

本章については、５年以内に

雑誌等で刊行予定のため、非公開

Chapter 5.

Concluding Remarks

5.1. Summary

My doctoral study is aimed to overcome the major challenges for polymer-stabilized metal clusters; atomically precise size control and determination of atomic structure. I successfully synthesized novel magic clusters of Au_{24}, $Au_{23}Pd_1$, and Au_{38} stabilized by polyvinylpyrrolidone (PVP) with atomic precision. Polydisperse and dynamic atomic structures of the clusters were observed. I demonstrated that size increase and single Pd atom doping significantly enhanced the catalytic activity for alcohol oxidation by promoting the hydride elimination (**Figure 5.1**).

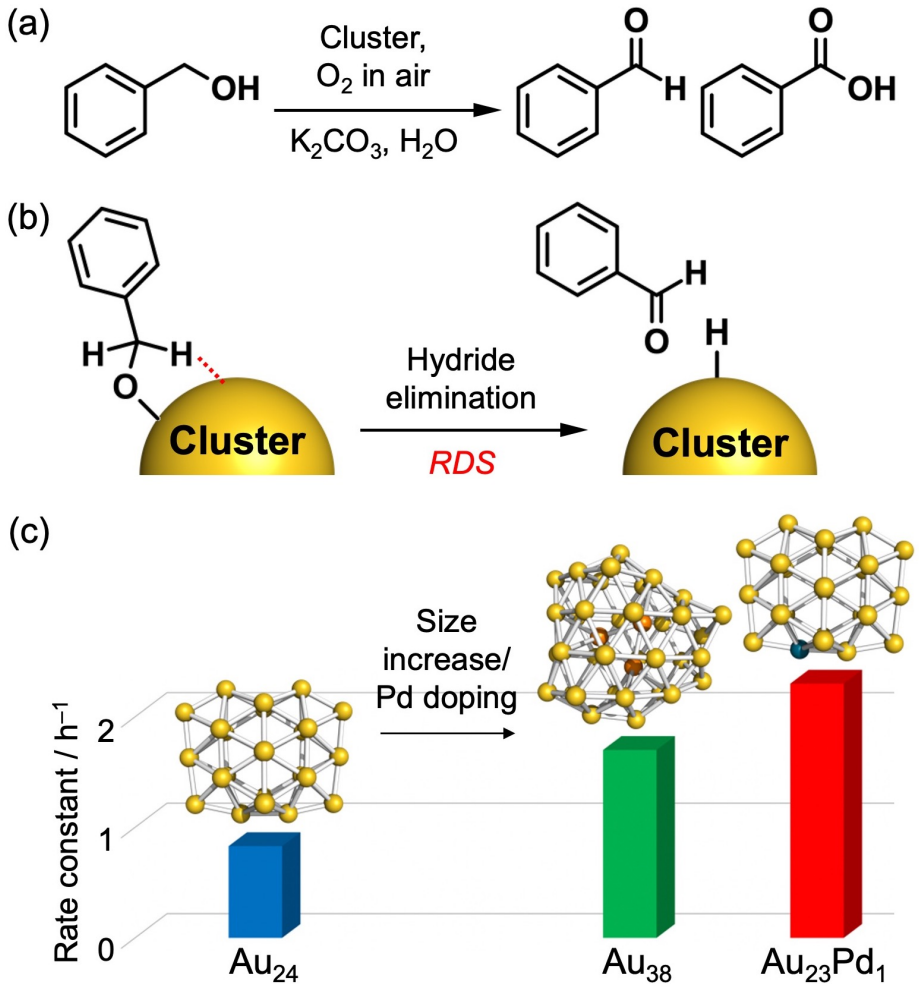

Figure 5.1. (a) Aerobic oxidation of benzyl alcohol catalyzed by clusters. (b) Rate-determining step (RDS) of the catalytic reaction. (c) Increase of reaction rate constant at 303 K caused by size increase and single Pd atom doping.

In Chapter 2, I achieved the atomically precise synthesis of a novel magic number cluster, Au_{24}:PVP, by the microfluidic mixing of reaction solutions containing a large excess of PVP. The successful synthesis was ascribed to the suppression of the growth reaction of clusters as well as the homogeneous mixing of the reaction solutions. By aberration-corrected transmission electron microscopic (ACTEM) video imaging of Au_{24}:PVP and TEM simulations of model Au_{24} clusters obtained by density functional theory (DFT) calculations, I revealed that Au_{24}:PVP was the mixture of structural isomers in which all the constituent atoms were exposed on the cluster surface. Furthermore, the dynamic nature of the atomic structure of Au_{24}:PVP was demonstrated by the direct observation of structural isomerization. I found that the metal core of Au_{24}:PVP was negatively charged due to the electron transfer from PVP, according to the results of X-ray photoelectron spectroscopy (XPS) and Fourier-transform infrared (FT-IR) spectroscopy of adsorbed carbon monoxide. The reaction mechanism of the aerobic oxidation of benzyl alcohol (**Figure 5.1a**) catalyzed by Au_{24}:PVP was investigated by kinetic measurements. I concluded that the rate-determining step of the catalytic oxidation was the hydride elimination from α-carbon by Au_{24}:PVP (**Figure 5.1b**), based on the observation of kinetic isotope effect (KIE) and substituent effects on reaction rate constants.

In Chapter 3, I demonstrated that single Pd atom could be doped into Au_{24}:PVP by the co-reduction method. $Au_{23}Pd_1$:PVP was selectively obtained by the reduction of the mixture of $HAuCl_4$ and Na_2PdCl_4 by $NaBH_4$ under the reaction condition similar to that for Au_{24}:PVP. I studied the local structure around the Pd dopant in $Au_{23}Pd_1$:PVP by Pd K-edge extended X-ray absorption fine structure (EXAFS) analysis, FT-IR spectroscopy of adsorbed carbon monoxide, and DFT calculations. Considering the coordination number

of the Pd–Au bond (6.1 ± 0.7) significantly smaller than 12 and the appearance of the absorption band corresponding to the CO adsorbed on Pd, I concluded that the Pd atom was exposed on the cluster surface. The single Pd atom doping effect on the catalysis was investigated for the benzyl alcohol oxidation. $Au_{23}Pd_1$:PVP showed the significantly higher catalytic activity; the reaction rate constant at 303 K for $Au_{23}Pd_1$:PVP (2.3 h^{-1}) was more than 2 times higher than that for Au_{24}:PVP (0.83 h^{-1}) and the apparent activation energy was reduced by single Pd atom doping from 56 ± 3 kJ mol^{-1} to 45 ± 2 kJ mol^{-1}. On the other hand, KIE suggested that the hydride elimination from the α-carbon of benzyl alcohol is also the rate-determining step for $Au_{23}Pd_1$:PVP. Based on the structure of $Au_{23}Pd_1$:PVP where the Pd atom is exposed on the surface and high affinity of Pd toward H, it is proposed that the Pd dopant acts as a reaction site for hydride elimination with reduced activation energy.

In Chapter 4, it was found that a new magic number cluster, Au_{38}:PVP, was selectively and reproducibly obtained by the size conversion reaction of the mixture of Au_{34} and Au_{43}. I revealed the polydisperse and dynamic nature of the atomic structure of Au_{38}:PVP by ACTEM video imaging with the help by the TEM simulation of DFT-optimized model structures. DFT calculations suggested the non-crystalline geometrical structures with 0–4 inner Au atoms as stable structural isomers. The catalytic activity of Au_{38}:PVP for the benzyl alcohol oxidation was significantly higher than that of Au_{24}:PVP. Au_{38}:PVP showed smaller apparent activation energy (48 ± 1 kJ mol^{-1}) than that of Au_{24}:PVP (56 ± 3 kJ mol^{-1}), whereas the KIE values of the clusters were comparable. This suggested that the hydride elimination is rate-determining step for both catalysts. Considering the higher adsorption energy of a hydride on an Au_{38} than on an Au_{24} revealed by DFT calculations, I proposed that the increased affinity of Au_{38} toward a hydride

contributes to the higher catalytic activity of Au_{38}:PVP for alcohol oxidation.

5.2. Future Prospects

In this thesis, I achieved the atomically precise size control of Au clusters stabilized by linear polymers for the first time. In Chapters 2 and 3, Au_{24}:PVP and $Au_{23}Pd_1$:PVP were synthesized by kinetically controlled reduction of metal precursor complexes using a micromixer and large amount of PVP, whereas Au_{38}:PVP was selectively produced by the size conversion of the mixture of Au_{34} and Au_{43}. Significant effects of single Pd atom doping and size increase on the catalytic activity of Au:PVP were demonstrated for the alcohol oxidation in Chapters 3 and 4. I revealed that the hydride elimination was the key step for the alcohol oxidation catalyzed by the clusters. Possible reasons for the enhanced catalytic activities were also described in the Chapters. Nevertheless, to elucidate the origin of doping and size effects, further insights should be obtained by kinetic studies using clusters with other compositions and sizes

Another possible method for the atomically precise synthesis of polymer-stabilized Au clusters is the controlled growth of Au clusters by sacrificial hydrogen reduction.[1] If adsorbed hydrogen atoms act as simple one-electron carriers for the electron counting of Au clusters,[2] a certain number of hydrogen atoms will be adsorbed on an Au cluster. Magic number Au clusters such as Au_{58} and Au_{70} will be obtained by the reduction of monovalent Au complexes by the adsorbed hydrogen atoms.[3] Recently, the controlled growth reactions of phosphine protected Au-based clusters, $[Au_9(PPh_3)_8]^{3+}$ and $[PdAu_8(PPh_3)_8]^{2+}$, have been reported.[4,5] The reactions were initiated by the two-electron doping by the adsorbed hydride provided by $NaBH_4$, followed by the addition of two AuCl units. The hydride-adsorbed intermediate clusters were observed by *in-situ*

electrospray ionization (ESI) mass spectrometry. These reports support the possibility of the atomically precise growth reaction of polymer-stabilized Au clusters. Furthermore, the sacrificial hydrogen reduction will also be effective for the control of the composition of polymer-stabilized bimetallic clusters. For example, $Au_{23}Pd_n$:PVP ($n > 1$) will be selectively obtained by the reduction of Pd ions by surface hydrogen under an appropriate reaction condition.

Synthesis using a dendrimer as a molecular template is also the versatile approach for atomically precise synthesis of metal clusters.[6,7] Dendrimers having a defined number of coordination sites for metal ions act as both templates for size-selective synthesis and stabilizers for resultant clusters. Yamamoto and co-workers have reported the precision synthesis of monometallic and alloy clusters using phenylazomethine dendrimers.

Mass spectrometry is an indispensable size evaluation method for atomically precise polymer-stabilized metal clusters to determine the sizes and compositions.[3,8–10] However, it has been applied to only Au and Au-based clusters among polymer-stabilized metal clusters. To extend the scope, soft ionization methods with wide applicability should be developed.

As demonstrated in Chapters 2 and 4, aberration corrected transmission electron microscopy (ACTEM) is a powerful tool to monitor the dynamic structure of polymer-stabilized metal clusters. By further improvements of measurement conditions and more efficient theoretical calculations, it will be possible to establish the energy landscape of polymer-stabilized metal clusters. Deep understanding of the potential energy surface is necessary to clarify the correlation between the structures and catalytic performances.

XAS is an effective method to obtain insights into the local structures and electronic states of specific elements contained in polymer-stabilized metal clusters.[11] In Chapter 3,

I revealed that the doped Pd atom of $Au_{23}Pd_1$:PVP was exposed on the cluster surface. *In-situ* or operando measurements of polymer-stabilized metal clusters under the conditions of catalytic reactions will provide deeper understanding of the reaction mechanism.

For practical catalytic applications of polymer-stabilized metal clusters, it is necessary to improve the stability and reusability of the clusters. Aoshima and co-workers reported that Au nanoparticles (4 nm) stabilized by vinyl ether star polymers, star(EOEOVE), worked as a robust and recyclable catalyst for the aerobic oxidation of alcohols.[12] Since star(EOEOVE) showed lower critical solution temperature type phase segregation behavior at ~40 °C, the polymer-stabilized Au nanoparticles could be easily separated from the reaction solution by raising the temperature. The recovered catalyst showed the catalytic activity similar to that of original one. Thus, the functionality of polymer-stabilized metal clusters can be improved by using a designed polymer.

References

1. Wang, Y.; Toshima, N. *J Phys. Chem. B* **1997**, *101*, 5301.
2. Walter, M.; Akola, J.; Lopez-Acevedo, O.; Jadzinsky, P. D.; Calero, G.; Ackerson, C. J.; Whetten, R. L.; Grönbeck, H.; Häkkinen, H. *Proc. Natl. Acad. Sci. U. S. A.* **2008**, *105*, 9157.
3. Tsunoyama, H.; Tsukuda, T. *J. Am. Chem. Soc.* **2009**, *131*, 18216.
4. Takano, S.; Hirai, H.; Muramatsu, S.; Tsukuda, T. *J. Am. Chem*. *Soc*. **2018**, *140*, 8380.
5. Takano, S.; Hirai, H.; Muramatsu, S.; Tsukuda, T. *J. Am. Chem. Soc.* **2018**, *140*, 12314.
6. Myers, V. S.; Weir, M. G.; Carino, E. V.; Yancey, D. F.; Pande, S.; Crooks, R. M. *Chem*. *Sci*. **2011**, *2*, 1632.
7. Yamamoto, K.; Imaoka, T.; Tanabe, M.; Kambe, T. *Chem. Rev.* **2020**, *120*, 1397.
8. Ishida, R.; Arii, S.; Kurashige, W.; Yamazoe, S.; Koyasu, K.; Negishi, Y.; Tsukuda, T. *Chin. J. Catal.* **2016**, *37*, 1656.
9. Hayashi, S.; Ishida, R.; Hasegawa, S.; Yamazoe, S.; Tsukuda, T. *Top. Catal.* **2018**, *61*, 136.
10. Hasegawa, S.; Takano, S.; Yamazoe, S.; Tsukuda, T. *Chem. Commun.* **2018**, *54*, 5915.
11. Yamazoe, S.; Tsukuda, T. *Bull. Chem. Soc. Jpn.* **2019**, *92*, 193.
12. Kanaoka, S.; Yagi, N.; Fukuyama, Y.; Aoshima, S.; Tsunoyama, H.; Tsukuda, T.; Sakurai, H. *J. Am. Chem. Soc.* **2007**, *129*, 12060.

List of Publications and Presentations

Publication comprising to the thesis

(Chapter 2)

1. "New Magic Au_{24} Cluster Stabilized by PVP: Selective Formation, Atomic Structure, and Oxidation Catalysis", Shingo Hasegawa, Shinjiro Takano, Koji Harano and Tatsuya Tsukuda, *JACS Au* **2021**, *1*, 660-668.

Publications not related to the thesis

1. "Exploring Novel Catalysis Using Polymer-Stabilized Metal Clusters", Shingo Hasegawa and Tatsuya Tsukuda, *Bull. Chem. Soc. Jpn.* **2021**, *94*, 1036-1044.

2. "Electron-Rich Gold Clusters Stabilized by Polyvinylpyridines as Robust and Active Oxidation Catalysts", Atsushi Matsuo, Shingo Hasegawa, Shinjiro Takano and Tatsuya Tsukuda, *Langmuir* **2020**, *36*, 7844-4849.

3. "Hydride Doping of Chemically Modified Gold-Based Superatoms", Shinjiro Takano, Shingo Hasegawa, Megumi Suyama and Tatsuya Tsukuda, *Acc. Chem. Res.* **2018**, *51*, 3074-3083.

4. "Prominent Hydrogenation Catalysis of a PVP-Stabilized Au_{34} Superatom Provided by Doping a Single Rh Atom", Shingo Hasegawa, Shinjiro Takano, Seiji Yamazoe and Tatsuya Tsukuda, *Chem. Commun.* **2018**, *54*, 5915-5918.

5. "Doping a Single Palladium Atom into Gold Superatoms Stabilized by PVP: Emergence of Hydrogenation Catalysis", Shun Hayashi, Ryo Ishida, Shingo Hasegawa, Seiji Yamazoe and Tatsuya Tsukuda, *Top. Catal.* **2018**, *61*, 136-141.

Oral presentations

1. “Structure and Oxidation Catalysis of PVP-Stabilized Au_{24} Cluster”, Shingo Hasegawa, Indo-Japan Virtual Workshop on Cluster Science by Interdisciplinary Approach: Emerging Materials and Phenomena, Online, September 2021. (招待講演)

2. “PVP 保護 Au_{24} クラスターの幾何構造と空気酸化触媒作用”, 長谷川慎吾, 高野慎二郎, 原野幸治, 佃達哉, ナノ学会第 19 回大会, オンライン開催, 2021 年 5 月.

3. “ポリマー保護金クラスターの原子精度合成と酸化触媒作用”, 長谷川慎吾, 高野慎二郎, 佃達哉, 分子科学会オンライン討論会, オンライン開催, 2020 年 9 月.

4. “原子精度でサイズ制御された PVP 保護金クラスターの触媒性能評価”, 長谷川慎吾, 高野慎二郎, 佃達哉, ナノ学会第 18 回大会, 神奈川, 2020 年 5 月.

5. “Effects of Stabilizing Polymers on Oxidation Catalysis of Gold Clusters”, Atsushi Matsuo, Shingo Hasegawa, Shinjiro Takano and Tatsuya Tsukuda, 日本化学会第 100 春季年会, 千葉, 2020 年 3 月.

6. “Size-Specific Aerobic Oxidation Catalysis of Atomically Precise Polymer-Stabilized Gold Clusters”, Shingo Hasegawa, Shinjiro Takano and Tatsuya Tsukuda, 日本化学会第 100 春季年会, 千葉, 2020 年 3 月.

Poster presentations

1. “PVP 保護金クラスターの原子精度合成と空気酸化触媒作用”, 長谷川慎吾, 高野慎二郎, 佃達哉, 第 126 回触媒討論会, オンライン開催, 2020 年 9 月. (学生ポスター発表賞)

2. “PVP 保護金クラスターの原子精度合成と触媒性能評価”, 長谷川慎吾, 高野慎二郎, 佃達哉, 第 125 回触媒討論会, 東京, 2020 年 3 月.

3. “Electron-Rich Gold Clusters Stabilized by Polyvinylpyridines as Robust and Active Oxidation Catalysts”, Atsushi Matsuo, Shingo Hasegawa, Shinjiro Takano and Tatsuya Tsukuda, Materials Research Meeting 2019, Yokohama, Japan, December 2019.

Acknowledgements

The presented works were carried out at Department Chemistry, Graduate School of Science, The University of Tokyo, under the supervision of Prof. Tatsuya Tsukuda. I deeply appreciate his guidance for five years. His kind advice contributed to making progress for my thesis. I learned what is required for a scientist from him; the fundamental knowledge of physical chemistry, the skills for writing and presentations, and the way to make research proposals. Without his patient help, my thesis would not have been possible.

I am deeply grateful to Prof. Seiji Yamazoe (Tokyo Metropolitan University), a former assistant professor of our group. During his career with our group, he especially taught me characterization techniques by X-ray absorption spectroscopy using synchrotron facilities. I would like to express my gratitude to Associate Prof. Kiichirou Koyasu for his instructions in gas phase experiments and theoretical calculations. I owe my thanks to Assistant Prof. Shinjiro Takano for his supports in liquid phase experiments. Also, my appreciation goes to Assistant Prof. Shinya Masuda for his advice on my research.

I would like to appreciate Associate Prof. Koji Harano (The University of Tokyo) for the access to TEM apparatus and valuable discussion on the structural analysis. I would like to thank Prof. Eiichi Nakamura (The University of Tokyo) for access to TEM apparatus. I am grateful to Mr. Ko Kamei (The University of Tokyo) for supporting TEM simulation.

I would like to thank Ms. Yuka Sakurai for her support of office works. I owe my thanks to the current laboratory members; Dr. Tsubasa Omoda, Mr. Sojiro Emori, Mr. Haru Hirai, Ms. Megumi Suyama, Mr. Katsunosuke Nakamura, Mr. Shun Ito, Mr. Taro Shigeta, Mr. Lewei, Wang, Ms. Emi Ito, Mr. Kensuke Eya, Mr. Toshiki Komagata, Ms. Yuriko Tasaka, Mr. Haruki Fukuda, Mr. Huang, Zengguang, Mr. Masashi Iwamoto, Mr. Naoki Kito, Mr. Kosuke Sakamoto, Mr. Takumi Imagawa, Mr. Masahiro Ogawa, Mr. Shuntaro Kunii, and Ms. Yuki Fujiwara. I am also grateful to former group members; Dr. Liang Feng, Dr. Ryo Takahata, Dr. Chun-Fu Chang, Dr. Satoru Muramatsu, Dr. Shun Hayashi, Dr. Ryohei Tomihara, Dr. Keisuke Hirata, Dr. Kazuyuki Tsuruoka, Mr. Naoto Sasaki, Mr. Daiki Shuto, Mr. Toshiaki Yanase, Mr. Hiroki Yamada, Mr. Hiroki Yamamoto, Mr. Lim Wei Loon, Mr. Kuenhee Kim, Mr. Naoaki Shinjo, Mr. Yuto Nakajima, Mr. Ray Horie, Ms. Atsuko Horinouchi, Mr. Junichi Yamazaki, Mr. Atsushi Matsuo, Mr. Satoshi Osugi, Mr. Takeki Konuma, Mr. Mizuki Shimojima, Ms. Koto Hirano, Mr. Shotaro Matsuda, Mr. Li Xiang and Ms. Lin I-Hsuan.

I appreciate the financial support from Japan Society for the Promotion of Science (JSPS) Research Fellowship for Young Scientists.

Finally I would like to thank my family for their support.

Shingo Hasegawa